



# Well-balanced High-order Finite Difference Weighted Essentially Nonoscillatory Schemes for a First-order Z4 Formulation of the Einstein Field Equations

Dinshaw Balsara<sup>1,2</sup> , Deepak Bhojia<sup>1</sup> , Olindo Zanotti<sup>3</sup> , and Michael Dumbser<sup>3</sup>

<sup>1</sup> Department of Physics and Astronomy, University of Notre Dame, Notre Dame, IN, USA; [dbalsara@nd.edu](mailto:dbalsara@nd.edu)

<sup>2</sup> ACMS Department, University of Notre Dame, Notre Dame, IN, USA

<sup>3</sup> Laboratory of Applied Mathematics, Department of Civil, Environmental and Mechanical Engineering, University of Trento, Via Mesiano 77, I-38123 Trento, Italy

Received 2024 June 18; revised 2024 September 18; accepted 2024 September 19; published 2024 November 8

## Abstract

We develop a new class of high-order accurate well-balanced finite difference (FD) weighted essentially nonoscillatory (WENO) methods for numerical general relativity (GR), which can be applied to any first-order reduction of the Einstein field equations, even if nonconservative terms are present. We choose the first-order nonconservative Z4 formulation of the Einstein equations, which has a built-in cleaning procedure that accounts for the Einstein constraints and that has already shown its ability in keeping stationary solutions stable over long timescales. By introducing auxiliary variables, the vacuum Einstein equations in first-order form constitute a partial differential equation system of 54 equations that is naturally nonconservative. We show how to design FD-WENO schemes that can handle nonconservative products. Different variants of FD WENO are discussed, with an eye to their suitability for higher-order accurate formulations for numerical GR. We successfully solve a set of fundamental tests of numerical GR with up to ninth-order spatial accuracy. Due to their intrinsic robustness, flexibility, and ease of implementation, FD-WENO schemes can effectively replace traditional central finite differencing in any first-order formulation of the Einstein field equations, without any artificial viscosity. When used in combination with *well-balancing*, the new numerical schemes preserve stationary equilibrium solutions of the Einstein equations exactly. This is particularly relevant in view of the numerical study of the quasi-normal modes of oscillations of relevant astrophysical sources. In conclusion, general relativistic high-energy astrophysics could benefit from this new class of numerical schemes and the ecosystem of desirable capabilities built around them.

*Unified Astronomy Thesaurus concepts:* General relativity (641); Einstein field equations (450); Computational methods (1965); Computational astronomy (293)

## 1. Introduction

In recent years, many of the equations that are needed in computational astrophysics have seen the development of higher-order methods for their solution. This harkens to the fact that the corresponding high accuracy is needed in response to more accurate observations; general relativity (GR) is an emblematic example of this fact. Indeed, the third generation of gravitational-wave detectors (H. Lück et al. 2022), such as the Einstein Telescope in Europe and the Cosmic Explorer in the US, with a planned sensitivity  $h$  in the range of  $10^{-25}$ – $10^{-24}$  Hz<sup>−1/2</sup>, will soon call for more accurate numerical solution methods in numerical relativity (NR).

As is well known, the Einstein equations present inbuilt challenges that do not show up in many of the other governing equations commonly considered in computational astrophysics. For one thing, the system naturally arises as a second-order partial differential equation (PDE) system, whereas our best numerical tools have been developed for first-order PDE systems. In this respect, it is interesting to note that while the generalized harmonic formulation has existed as a first-order system for quite a while (L. Lindblom et al. 2006), having already allowed for highly relevant scientific results (see, among others, M. Boyle et al. 2007; M. D. Duez et al. 2008; M. A. Scheel et al. 2009; B. Szilágyi 2014; W. Tichy et al. 2023; N. Deppe et al. 2024

and references therein), the whole family represented by the BSSNOK/Z4/CCZ4 formulations (T. Nakamura et al. 1987; M. Shibata & T. Nakamura 1995; T. W. Baumgarte & S. L. Shapiro 1998, 2010; C. Bona & C. Palenzuela-Luque 2005; M. Alcubierre 2008; D. Alic et al. 2009) seems to have shown stronger inertia in performing the transition from second-order to first-order implementations, with notable but rare progress reported by C. Bona et al. (2004), J. D. Brown et al. (2012), and M. Dumbser et al. (2018). The latter, in particular, applied discontinuous-Galerkin (DG) schemes to the conformal and covariant Z4 formulation of the Einstein equations (FO-CCZ4) of D. Alic et al. (2012). More recently, M. Dumbser et al. (2024) obtained promising results after using DG methods in a well-balanced first-order implementation of the damped version of the Z4 formulation proposed by C. Gundlach et al. (2005), henceforth referred to as the FO-Z4 formulation. We recall that the Z4 formulation of the Einstein equations was originally proposed by C. Bona et al. (2003, 2004) to automatically account for proper treatment of the Einstein constraints through the addition of a four vector  $z^\mu$ , in a rather similar way to what is done in the divergence cleaning approach by C.-D. Munz et al. (2000) and A. Dedner et al. (2002) for the Maxwell and magnetohydrodynamic equations. Later on, this approach was combined with the conformal decomposition of the metric, which is missing in the original Z4 formulation, to obtain the so-called CCZ4 and Z4c formulations (D. Alic et al. 2012, 2013; D. Hilditch & R. Richter 2012; D. Hilditch et al. 2013; M. Dumbser et al. 2018; A. J. Peterson et al. 2023).



Original content from this work may be used under the terms of the [Creative Commons Attribution 4.0 licence](https://creativecommons.org/licenses/by/4.0/). Any further distribution of this work must maintain attribution to the author(s) and the title of the work, journal citation and DOI.

On the computational side, one can expect that, for various reasons, finite difference (FD) schemes will remain the preferred choice by the NR community still for many years to come. When a second-order formulation of the Einstein equations is adopted, central FD schemes are the most natural choice, which is indeed the case for such popular codes such as the Einstein Toolkit (F. Löffler et al. 2012), LazEv (Y. Zlochower et al. 2005; C. O. Lousto & J. Healy 2023), BAM (B. Brügmann et al. 2008; M. Thierfelder et al. 2011), McLachlan,<sup>4</sup> GRChombo (K. Clough et al. 2015), AMReX (A. J. Peterson et al. 2023), and SACRA (T. Yamamoto et al. 2008; K. Kiuchi et al. 2017). On the other hand, when a first-order formulation of the Einstein equations is available, a natural temptation arises, namely, to migrate from central FD schemes to FD-weighted essentially nonoscillatory (WENO) methods, due to their superior robustness in the presence of shock waves and singularities, maintaining at the same time an excellent performance in terms of accuracy. However, original WENO methods were specifically devised for first-order hyperbolic systems *in conservation form*, and they do therefore not fit straightforwardly into the nonconservative form of the first-order Einstein equations. In fact, the usage of FD-WENO methods in the relativistic context has been so far limited to the solution of the (conservative) term  $\nabla_\mu T^{\mu\nu} = 0$ , either in special relativity or in general relativistic but stationary spacetimes (L. Del Zanna et al. 2007; K. Wu & H. Tang 2015; G. Inghirami et al. 2016). It is interesting to note that the Z4 formulation of the Einstein equations was actually originally proposed in first-order conservative form (C. Bona et al. 2004; C. Bona & C. Palenzuela-Luque 2005), though it does not seem that it has ever been implemented by using FD-WENO methods.

As we have just discussed, the very large size of the FO-Z4 system, as well as its nonconservative aspect, restricts our choice of numerical methods that can be applied to it. As realized in M. Dumbser et al. (2018, 2020) and M. Dumbser et al. (2024), path-conservative DG schemes may be one route to higher order for the Einstein equations, but DG schemes tend to be prohibitively expensive, both in terms of their memory usage as well as in terms of computational complexity. This is because a DG scheme retains all the higher-order modes of a hyperbolic system, and for a gigantic hyperbolic system, like the one being considered, that exacerbates the memory consumption. All these modes also have to be evolved in time with the result that the computational complexity of evaluating so many evolutionary equations for each of the modes of a DG scheme can again become prohibitive. Finite-volume WENO schemes are another alternative route to higher order and recently some efficient options have been offered, see D. S. Balsara et al. (2023b), and the supplement of that paper, as well as M. Dumbser et al. (2013). However, the finite-volume WENO schemes require the reconstruction of the same number of modes as a DG scheme of the same order. Consequently, finite-volume WENO schemes also have a prohibitive memory usage, though their computational complexity and time-step restriction are much better than DG schemes of the same order. The only remaining path to high-order accuracy at low computational cost is therefore through FD-WENO schemes (C.-W. Shu & S. Osher 1988, 1989; G.-S. Jiang & C.-W. Shu 1996; D. S. Balsara & C.-W. Shu 2000; D. S. Balsara et al. 2016, 2023a, 2024a, 2024b). Compared to

their finite volume and DG cousins, FD schemes have a memory usage and computational complexity that can be described as downright Spartan. Unlike DG schemes, they offer a robust Courant–Friedrichs–Lewy (CFL) even at higher orders. As shown in D. S. Balsara et al. (2024b), the ninth-order FD-WENO schemes are not much more expensive compared to their third-order variants, with the result that the path to progressively higher order does not incur much additional expense in terms of computational complexity. This owes to the dimension-by-dimension approach that is used in FD-WENO schemes.

It is worth noting that there are two variants of FD-WENO schemes. The well-known one, which we can refer to as the classical FD-WENO scheme (here referred to as FD-WENO) stems from C.-W. Shu & S. Osher (1989). For a long time, it was only available in a form that was suitable for conservation laws. In that form, it is quite useless for first-order nonconservative formulations of the Einstein equations, such as those considered by M. Dumbser et al. (2018, 2024) or J. D. Brown et al. (2012). Recently, the FD-WENO schemes have also been extended to hyperbolic PDE systems with nonconservative products (D. S. Balsara et al. 2023a). In a paper that slightly predates C.-W. Shu & S. Osher (1988, 1989) also presented an alternative formulation of FD-WENO schemes, but for a long time these methods had remained inaccessible to the broader community. This is partly owing to the mathematically recondite nature of the original presentation and partly owing to the fact that the original formulation in C.-W. Shu & S. Osher (1988) was far from broadly usable. We will refer to this alternative strain of FD-WENO schemes as the alternative finite difference (AFD)-WENO schemes. The original AFD-WENO schemes were, therefore, eclipsed by the vastly more popular FD-WENO schemes. A paper by B. Merriman (2003) tried to make the underlying mathematics of the AFD-WENO schemes more accessible. These days, of course, the mathematics that underlies AFD-WENO schemes has become very accessible; please see Section 2 in D. S. Balsara et al. (2024a) as well as their Appendix A, which provides a computer algebra system-based derivation of the scheme. The impetus for AFD-WENO schemes came when X. Cai & F. Ladeinde (2008) and T. Nonomura et al. (2010) showed that FD-WENO schemes could not preserve a free stream condition on geometrically complex meshes. In Y. Jiang et al. (2013, 2014), it was realized that FD-WENO suffered from an inability to preserve a free stream condition because it was based on flux reconstruction. AFD-WENO schemes were found to be free of such limitations. However, even in F. Zheng et al. (2021), controlling the Gibbs phenomenon that arises from the higher-order flux derivatives in AFD-WENO was found to be an elusive enterprise. A full resolution of controlling the Gibbs phenomenon only emerged in D. S. Balsara et al. (2024a), where a different type of WENO interpolation was invented for that purpose. The paper by D. S. Balsara et al. (2024a) still presented AFD-WENO schemes for conservation laws. The extension of these AFD-WENO methods to hyperbolic systems with nonconservative products was finally accomplished in D. S. Balsara et al. (2024b). The upshot of this paragraph is that we now have two very proficient methods for treating hyperbolic PDEs with a large number of nonconservative products, such as those that arise in NR. We have the FD-WENO methods from D. S. Balsara et al. (2023a) and we have the AFD-WENO methods from D. S. Balsara et al. (2024b).

<sup>4</sup> <http://www.cct.lsu.edu/~eschnett/McLachlan/>

Modern astrophysical codes rely on capabilities that go beyond the baseline scheme. A good example would be well-balancing, which makes it possible to approach a steady state on moderately resolved meshes; see R. Kappeli (2022) for a review and E. Gaburro et al. (2021) for a first successful application of well-balancing to numerical GR. Because FD-WENO schemes in conservation form have been around for a while, well-balancing has been developed for these methods (Y. Xing & C.-W. Shu 2011). In D. S. Balsara et al. (2023a), we showed that FD-WENO schemes for nonconservative products also tend to be well balanced if contact-discontinuity preserving Riemann solvers are used. For AFD-WENO schemes in conservation form, Z. Xu & C.-W. Shu (2024, in preparation) have shown that they can be formulated so as to be well balanced and can also preserve moving equilibria provided one is willing to go through the cumbersome process of identifying those equilibria. In recent work, we have seen the development of well-balanced methods that preserve moving equilibria (Z. Xu & C.-W. Shu 2024, in preparation). Another capability that goes beyond the baseline scheme is positivity preservation, which is also referred to these days as the physical condition preserving (PCP) property. For FD-WENO schemes in conservation form, X. Y. Hu et al. (2013) have developed positivity-preserving formulations. This author and his collaborators have also developed PCP formulations for AFD-WENO schemes (D. Bhoriya et al. 2024). Astrophysical codes also have geometrical constraints that require divergence preservation (D. S. Balsara & D. S. Spicer 1999; D. S. Balsara 2010, 2012, 2014) and curl preservation (D. S. Balsara et al. 2021; D. S. Balsara & R. Käppeli 2022) and the author and his collaborators are extending these capabilities to include AFD-WENO methods. We see, therefore, that there is an ecosystem of ancillary algorithms that have been built, and are being built, around methods that make them very useful for NR.

The plan of this paper is the following. In Section 2 we recall the essential features of the first-order Z4 formulation of the Einstein field equations. Section 3 contains the core novelties of this paper by presenting a new class of FD-WENO schemes, whose validation is reported in Section 4. Finally, Section 5 contains the conclusions of our work.

We assume a signature  $\{-, +, +, +\}$  for the spacetime metric, and we use the Greek letters  $\mu, \nu, \lambda, \dots$  (running from 0 to 3) for four-dimensional spacetime tensor components, while Latin letters  $i, j, k, \dots$  (running from 1 to 3) are employed for three-dimensional spatial tensor components. Moreover, we set  $G = c = 1$ .

## 2. The Damped First-order Z4 System of the Einstein Equations

As usual for 3+1 formulations of the Einstein equations, the spacetime is foliated through  $\Sigma_t = \text{const}$  hypersurfaces as (M. Alcubierre 2008; T. W. Baumgarte & S. L. Shapiro 2010; E.ourgoulhon 2012; L. Rezzolla & O. Zanotti 2013)

$$ds^2 = g_{\mu\nu} dx^\mu dx^\nu = -(\alpha^2 - \beta_i \beta^i) dt^2 + 2\beta_i dx^i dt + \gamma_{ij} dx^i dx^j, \quad (1)$$

where  $g_{\mu\nu}$  is the spacetime metric tensor,  $\alpha$  is the lapse,  $\beta^i$  is the shift, and  $\gamma_{ij}$  is the metric of the three-dimensional space. Within this framework, we adopt the damped version of the Z4 formulation of the vacuum Einstein equations, originally

proposed by C. Gundlach et al. (2005) and recently reformulated with minor modifications by M. Dumbser et al. (2024), i.e.,

$$G_{\mu\nu} + \nabla_\mu z_\nu + \nabla_\nu z_\mu - \nabla_\pi z^\pi g_{\mu\nu} - \kappa_1(n_\mu z_\nu + n_\nu z_\mu) - \kappa_2 n_\pi z^\pi g_{\mu\nu} = 0, \quad (2)$$

where  $G_{\mu\nu}$  is the Einstein tensor and  $n^\mu$  is the four velocity of the Eulerian observer. The four vector  $z^\mu = \Theta n^\mu + Z^\mu$  is artificially introduced to *clean* the violations of the Einstein constraints. We therefore notice that  $\Theta$  and  $Z^\mu$  are the 3+1 representations of  $z^\mu$ . The two constant coefficients  $\kappa_1$  and  $\kappa_2$  can act as damping mechanisms over the four vector  $z^\mu$ . Not present in the original formulation by C. Bona et al. (2003, 2004), such coefficients were introduced by C. Gundlach et al. (2005) and slightly modified by M. Dumbser et al. (2024) in such a way as to avoid their mutual multiplication in the resulting PDE system. The *extrinsic curvature* of the hypersurface  $\Sigma_t$ , a crucial quantity of differential geometry, is one of the primary variables of the Z4 formulation and it is defined as

$$K_{\mu\nu} = -\gamma^\alpha_\mu \nabla_\alpha n_\nu = -\nabla_\mu n_\nu - n_\mu a_\nu, \quad (3)$$

where  $a_\mu = n^\nu \nabla_\nu n_\mu$  is the acceleration of the Eulerian observer. Upon the introduction of 30 auxiliary variables involving first derivatives of the metric terms, namely,

$$A_i := \partial_i \ln \alpha = \frac{\partial_i \alpha}{\alpha}, \quad B_k^i := \partial_k \beta^i, \quad D_{kij} := \frac{1}{2} \partial_k \gamma_{ij}, \quad (4)$$

and after fixing the gauge conditions in a pretty standard way as (J. A. Faber et al. 2007; T. W. Baumgarte & S. L. Shapiro 2010)

$$\partial_i \ln \alpha - \beta^k \partial_k \ln \alpha = -g(\alpha) \alpha (K - K_0 - 2c\Theta), \quad (5)$$

$$\partial_i \beta^i = \frac{3}{4} b^i, \quad (6)$$

$$\partial_i b^i = \partial_i \hat{\Gamma}^i - \eta b^i, \quad (7)$$

the vacuum Einstein equation, Equation (2), leads to the following first-order system of hyperbolic PDEs:

$$\partial_t \gamma_{ij} - \beta^k \partial_k \gamma_{ij} = \gamma_{ik} B_j^k + \gamma_{kj} B_i^k - 2\alpha K_{ij}, \quad (8)$$

$$\begin{aligned} \partial_t K_{ij} - \beta^k \partial_k K_{ij} + \alpha \partial_{(i} A_{j)} - \alpha \gamma^{kl} (\partial_{(k} D_{l)ij} - \partial_{(i} D_{l)j}) \\ + \alpha \gamma^{kl} (\partial_{(j} D_{i)kl} - \partial_{(j} D_{i)lk}) - 2\alpha \partial_{(i} Z_{j)} = K_{ki} B_j^k + K_{kj} B_i^k \\ - \alpha A_i A_j + \alpha \Gamma_{ij}^k A_k + \alpha [-2\gamma^{kn} \gamma^{pl} D_{knp} (D_{ijl} + D_{jil} - D_{lij}) \\ + 2\gamma^{kn} \gamma^{pl} D_{jnp} (D_{ikl} + D_{kil} - D_{lik}) \\ + \Gamma_{lm}^m \Gamma_{ij}^l - \Gamma_{lj}^m \Gamma_{im}^l] - 2\alpha \Gamma_{ij}^k Z_k - \alpha \Theta \gamma_{ij} (\kappa_1 + \kappa_2) \\ - 2\alpha K_{il} \gamma^{lm} K_{mj} + \alpha K_{ij} (K - 2\Theta), \end{aligned} \quad (9)$$



$$\begin{aligned}
\partial_t \Theta - \beta^k \partial_k \Theta - \frac{1}{2} \alpha e^2 [\gamma^{ij} \gamma^{kl} (\partial_{(k} D_{i)jl} - \partial_{(k} D_{l)ij}) \\
- \gamma^{ij} \gamma^{kl} (\partial_{(j} D_{i)kl} - \partial_{(j} D_{l)ik}) + 2 \gamma^{ij} \partial_i Z_j] \\
= \frac{\alpha}{2} e^2 [-2 \gamma^{ij} \gamma^{kn} \gamma^{pl} D_{knp} (D_{ijl} + D_{jil} - D_{lij}) \\
+ 2 \gamma^{ij} \gamma^{kn} \gamma^{pl} D_{jnp} (D_{ikl} + D_{kil} - D_{lik}) \\
+ \gamma^{ij} (\Gamma_{lm}^m \Gamma_{ij}^l - \Gamma_{lj}^m \Gamma_{im}^l) + K^2 - K_{ij} K^{ij}] \\
+ \alpha [-\gamma^{ij} \Gamma_{ij}^k Z_k - Z^k A_k] - \alpha \Theta K - \alpha \Theta (2\kappa_1 + \kappa_2), \quad (10)
\end{aligned}$$

$$\begin{aligned}
\partial_t Z_i - \beta^k \partial_k Z_i - \alpha \partial_i \Theta - \alpha [\gamma^{jm} \partial_j K_{mi} - \gamma^{mn} \partial_i K_{mn}] \\
= Z_k B_i^k + \alpha [-\gamma^{jm} (\Gamma_{jm}^n K_{ni} + \Gamma_{ji}^n K_{mn}) \\
+ \gamma^{mn} (\Gamma_{im}^l K_{ln} + \Gamma_{in}^l K_{ml})] + \alpha [-2 K_i^j Z_j - \Theta A_i - \kappa_1 Z_i], \quad (11)
\end{aligned}$$

$$\begin{aligned}
\partial_t A_i - \beta^k \partial_k A_i + \alpha g(\alpha) (\gamma^{mn} \partial_i K_{mn} - \partial_i K_0 - 2c \partial_i \Theta) \\
= -\alpha A_i (K - K_0 - 2\Theta c) (g(\alpha) + \alpha g'(\alpha)) \quad (12)
\end{aligned}$$

$$+ 2\alpha g(\alpha) K^{jk} D_{ijk} + B_i^k A_k, \quad (13)$$

$$\partial_t B_k^i - s \left( \frac{3}{4} \partial_k b^i - \alpha^2 \mu \gamma^{ij} \gamma^{nl} (\partial_k D_{ljn} - \partial_l D_{kjn}) \right) = 0, \quad (14)$$

$$\begin{aligned}
\partial_t D_{kij} - \beta^l \partial_l D_{kij} - \frac{1}{2} \gamma_{mi} \partial_k B_j^m - \frac{1}{2} \gamma_{mj} \partial_k B_i^m + \alpha \partial_k K_{ij} \\
= B_k^m D_{mij} + B_j^m D_{kmi} + B_i^m D_{kmj} - \alpha A_k K_{ij}. \quad (15)
\end{aligned}$$

Equations (8)–(15), augmented by the gauge conditions, Equations (5)–(7), form a nonconservative system which can be written as

$$\begin{aligned}
\frac{\partial \mathbf{U}}{\partial t} + \mathbf{A}_i(\mathbf{U}) \frac{\partial \mathbf{U}}{\partial x_i} = \mathbf{S}(\mathbf{U}), \quad \text{or, equivalently,} \\
\frac{\partial \mathbf{U}}{\partial t} + \mathbf{A}(\mathbf{U}) \cdot \nabla \mathbf{U} = \mathbf{S}(\mathbf{U}), \quad (16)
\end{aligned}$$

where  $\mathbf{U}$  is the state vector, composed of 54 dynamical variables, i.e., 10 for the lapse, the shift vector and the metric components, six for  $K_{ij}$ , three for the three vector  $Z_i$ , one for the scalar  $\Theta$ , three for  $A_i$ , nine for  $B_i^j$ , 18 for  $D_{ijk}$ , one for  $K_0$ , and three for  $b^i$ . The source term  $\mathbf{S}(\mathbf{U})$  contains algebraic terms only. The hyperbolic nature of Equation (16) has been proved by M. Dumbser et al. (2024) after a careful analysis of the matrix  $\mathbf{A}(\mathbf{U})$  via mathematical software packages, and the interested reader is pointed to that work, and especially the Appendix in that work, for further details. We just recall here that, as already noticed by M. Dumbser et al. (2018), hyperbolicity is helped by moving any spatial derivatives of the metric terms  $\alpha$ ,  $\beta^i$ , and  $\gamma_{ij}$  to the right-hand side via the auxiliary variables, Equation (4).

A few additional comments regarding the terms entering Equations (8)–(15) are worth giving.

1.  $\Gamma_{jk}^i = \gamma^{kl} (D_{ijl} + D_{jil} - D_{lij})$  are the Christoffel symbols of the spatial metric  $\gamma_{ij}$ .
2.  $K$  in Equation (5) (and elsewhere) is the trace of the extrinsic curvature, but it is not a primary variable, i.e., it does not belong to the vector  $\mathbf{U}$ .

3. The function  $g(\alpha)$  in Equation (5) is set to  $g(\alpha) = 2/\alpha$  for the *1+log gauge condition*, and to  $g(\alpha) = 1$  for the *harmonic gauge condition*.
4. The factor  $c$  in Equation (5) (and elsewhere) is always zero, except for the test of the gauge wave discussed in Section 4.1.
5. The factor  $s$  in Equation (14), either 1 or 0, is used to switch the *gamma driver* on or off.
6. The quantities  $\hat{\Gamma}^i$  in Equation (7) for the gamma driver are defined as  $\hat{\Gamma}^i = \gamma^{jk} \Gamma_{jk}^i + 2\gamma^{ij} Z_j$ , but they are not primary variables. Hence, their evolution is obtained from that of the primary variables, i.e.,

$$\begin{aligned}
\partial_t \Gamma_{jk}^i = \gamma^{im} \beta^r [\partial_r D_{jmk} + \partial_r D_{kjm} - \partial_r D_{mjk}] \\
+ \partial_{(j} B_{k)}^i - \alpha \gamma^{im} (\partial_j K_{mk} + \partial_k K_{jm} - \partial_m K_{jk}) \\
+ \gamma^{im} [D_{jmn} B_k^n + D_{nmk} B_j^n + D_{knm} B_j^n \\
+ D_{njm} B_k^n - D_{mjn} B_k^n - D_{mnk} B_j^n] \\
- \alpha \gamma^{im} (A_j K_{mk} + A_k K_{jm} - A_m K_{jk}) \\
+ [-2\gamma^{ip} \gamma^{mq} \beta^r D_{rpq} - \gamma^{mr} B_r^i + 2\alpha \gamma^{ip} \gamma^{mq} K_{pq}] \\
\times (D_{jmk} + D_{kjm} - D_{mjk}). \quad (17)
\end{aligned}$$

7. The factor  $\eta$  in Equation (7) is a damping parameter for the gamma driver.
8. The factor  $e$  in Equation (10) is the cleaning speed of the Einstein energy constraint.
9. The factor  $\mu$  in Equation (14) is used to insert a curl-free term that is zero on the continuum level, but that favors hyperbolicity of the whole PDE system.

We are now in a position to address the discretization of the system, Equation (16), via FD-WENO schemes, to which Section 3 is entirely devoted.

### 3. A Consideration of Several FD-WENO Schemes as They Pertain to NR

We had briefly mentioned that FD-WENO schemes offer the threefold advantages of very high accuracy, very low memory usage and low computational complexity. To use them well, and also to make decisions about their strengths and weaknesses, it is very important to understand the FD-WENO philosophy very briefly and why it offers these threefold benefits. Consider, therefore, the finite-volume schemes that are quite common in computational astrophysics. They all start with a volume-averaged representation of the solution vector in each zone. By polling the neighboring zones, a multidimensional high-order finite-volume scheme will use WENO reconstruction to build all the higher-order moments in multiple dimensions. As the order of accuracy increases, the number of moments with cross terms that have to be built also increases. By contrast, consider an FD approach to a simple one-dimensional conservation law, which we write as

$$\partial_t U + \partial_x F(U) = 0 \iff \partial_t U = -\partial_x F(U). \quad (18)$$

An FD scheme will start with a mesh function,  $\{U_i\}$ , that is provided in the form of point values of the solution vector at each of the zone centers “ $i$ .” Here, we assume a uniform mesh with zones of size  $\Delta x$ , taking time steps of size  $\Delta t$ . Because we are starting with point values, the FD scheme requires us to accurately evaluate the gradient  $\partial_x F(U)$  at that same zone-



centered point. The transcription to multiple dimensions is, therefore, very easy because we simply want all the flux gradients in all three directions to be evaluated at the same point with sufficiently high accuracy. This shows us that FD schemes operate on a dimension-by-dimension basis. This is the reason why it was acceptable to only show Equation (18) in one dimension because additional dimensions only contribute additively. Unlike high-order finite-volume approaches, where a 3D finite-volume scheme can be substantially more than three times costlier than a one-dimensional scheme, a 3D FD scheme will only be three times costlier than a one-dimensional one. We also see that the memory usage is very favorable for FD schemes. This is because we do not need to reconstruct all the higher-order moments in all dimensions and store them in computer memory, as we would do for a finite-volume scheme. An FD scheme only needs to retain the point values of the solution vector at the zone centers. Any higher moments that are needed will only be needed in a dimension-by-dimension fashion and can be discarded from computer memory once that dimension has been processed. By the same token, it is also possible to show that the computational complexity of an FD-WENO scheme does not increase by much as one progresses to higher orders of spatial accuracy; please see Table 5 in Section 5.4 of D. S. Balsara et al. (2024b).

Now that the advantages of FD-WENO have been documented, we provide very brief descriptions of these schemes here so that the reader has sufficient background, concentrated all in one place, with which to understand these schemes as they will be used for the FO-Z4 system from Section 2.

### 3.1. FD-WENO Schemes for Conservation Laws

Although our immediate goal is not to understand conservation laws, it helps to quickly document the WENO philosophy that led to FD-WENO schemes for conservation laws. (Without an understanding of conservation laws, it is impossible to understand systems in nonconservative form.) The primary goal of FD-WENO for conservation laws is to try and write Equation (18) for any zone “ $i$ ” on a one-dimensional mesh as

$$\partial_t U_i = - \frac{\hat{F}_{i+1/2} - \hat{F}_{i-1/2}}{\Delta x}. \quad (19)$$

Here,  $\hat{F}_{i+1/2}$  and  $\hat{F}_{i-1/2}$  are the reconstructed numerical fluxes at the zone boundaries  $x_i + \Delta x/2$  and  $x_i - \Delta x/2$ . For this to work out as a viable high-order scheme, we need the finite difference approximation (FDA) given by  $(\hat{F}_{i+1/2} - \hat{F}_{i-1/2})/\Delta x$  to approximate  $(\partial_x F)_i$  with a very high order of accuracy. Therefore, the problem can be stated as follows. We have to start with the so-called *physical fluxes* evaluated from the point values on the mesh, i.e.,  $\{F(U_i)\}$ , and obtain *numerical fluxes* such that  $(\hat{F}_{i+1/2} - \hat{F}_{i-1/2})/\Delta x = (\partial_x F)_i + O(\Delta x^k)$  for a spatially  $k$ th-order accurate scheme.

The denouement of the previously posed problem comes from the fundamental theorem of integral calculus, as was first realized by C.-W. Shu & S. Osher (1989). Consider a function  $f(x)$  that is defined in terms of another functional  $\mathcal{F}(\xi)$  as

follows:

$$f(x) \equiv \frac{1}{\Delta x} \int_{x-\Delta x/2}^{x+\Delta x/2} \mathcal{F}(\xi) d\xi. \quad (20)$$

Then, the fundamental theorem of integral calculus tells us that

$$(\partial_x f)|_{x=x_i} = \frac{1}{\Delta x} \left[ \mathcal{F}\left(x_i + \frac{\Delta x}{2}\right) - \mathcal{F}\left(x_i - \frac{\Delta x}{2}\right) \right]. \quad (21)$$

We see, therefore, that the left-hand side of Equation (21) is exactly of the same form as the right-hand side of the second equation in Equation (18), whereas the right-hand side of Equation (21) is exactly of the same form as the right-hand side of Equation (19). We have, therefore, found a way of connecting the gradient in Equation (18) to the FDA in Equation (19). Consequently, we seek a function  $\mathcal{F}(\xi)$  whose value  $\mathcal{F}(x_{i+1/2})$  at the zone boundary approximates  $\hat{F}_{i+1/2}$  with a sufficiently high order of accuracy. Now, the very familiar problem of “reconstruction by primitive” that was introduced in P. Colella & P. R. Woodward (1984) (and extended to ENO schemes with accreditation in A. Harten et al. 1986) comes to the rescue. It says that the reconstruction polynomial for the zone boundary “ $i + 1/2$ ” that we seek should be such that it matches the condition

$$\int_{\xi=x_{i-j}-\Delta x/2}^{\xi=x_{i-j}+\Delta x/2} \mathcal{F}(\xi) d\xi = \Delta x F(U_{i-j}) \quad (22)$$

for some zones “ $j$ ” that are adjacent to the zone boundary “ $i + 1/2$ ” under consideration. If the polynomial is chosen to be of sufficient order of accuracy, the task that was identified in the previous paragraph is accomplished. We can make the polynomial sufficiently accurate by making the stencil operations alluded to in Equation (22) wide enough. We choose  $\mathcal{F}(\xi)$  to be a consistent polynomial that is of degree “ $k - 1$ ” in order to obtain a  $k$ th-order accurate scheme. This polynomial will be pinned down more precisely in subsequent paragraphs.

While the process of identifying the polynomial associated with reconstructing the fluxes was described in the previous paragraph, more is needed in order to obtain a successful scheme. Such a scheme needs to be upwinded and the reconstruction process that was briefly described in Equation (22) needs to be based on nonlinear hybridization. To appreciate the concept of upwinding, realize that any flux “ $F(U)$ ” can be split as

$$\begin{aligned} F(U) &= \frac{1}{2}(F(U) + S U) + \frac{1}{2}(F(U) - S U) \\ &= F^+(U) + F^-(U), \end{aligned} \quad (23)$$

with the definitions

$$\begin{aligned} F^+(U) &\equiv \frac{1}{2}(F(U) + S U) \text{ and} \\ F^-(U) &\equiv \frac{1}{2}(F(U) - S U). \end{aligned} \quad (24)$$

Here, the wave speed “ $S$ ” is the maximum of the absolute values of all the signal speeds from the flux. This choice of “ $S$ ” ensures that the Jacobian  $\partial F^+(U)/\partial U$  will always have nonnegative eigenvalues and the Jacobian  $\partial F^-(U)/\partial U$  will always have nonpositive eigenvalues. (As a shorthand, we will

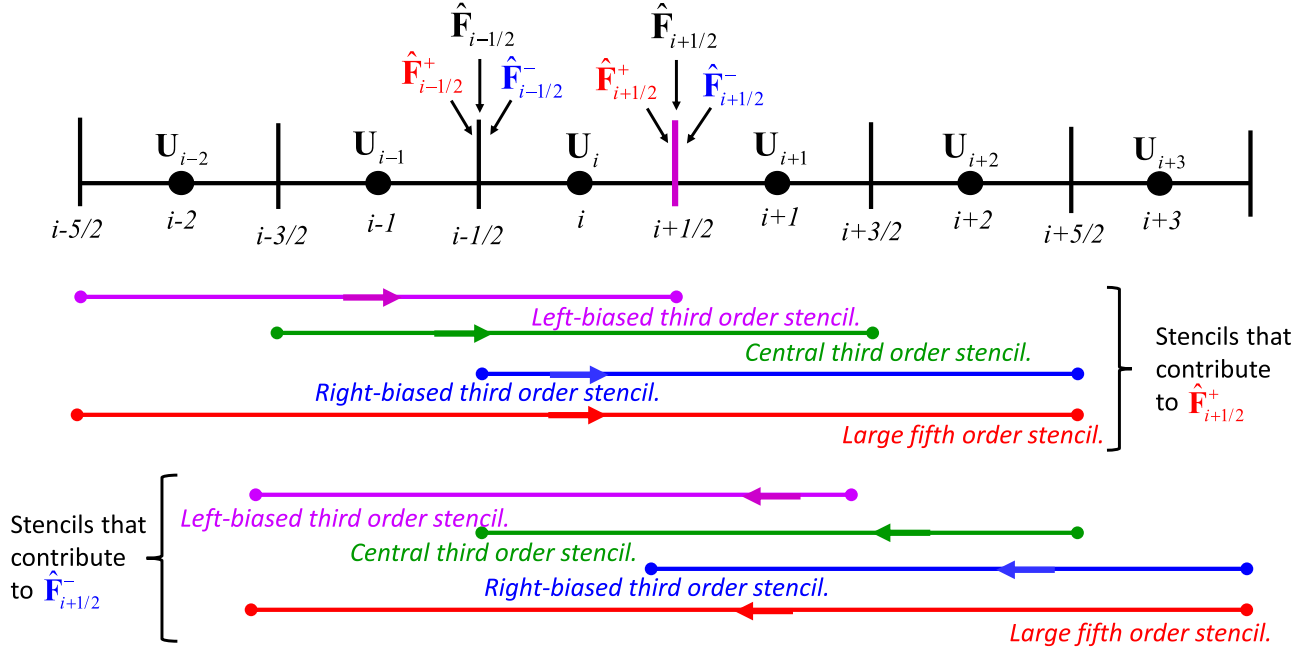


**Figure 1.** The schematic structure of a fifth-order FD-WENO scheme in conservation form. Please focus on the purple zone boundary at  $i + 1/2$ . The numerical flux at that zone boundary is made up of two split flux contributions  $F^+$  and  $F^-$ . The stencils contributing to the reconstruction of the right-going flux  $F^+$  at the purple zone boundary are shown. The stencils contributing to the reconstruction of the left-going flux  $F^-$  at the purple zone boundary are also shown.

often use  $F^+(U) \rightarrow F^+$  and  $F^-(U) \rightarrow F^-$ .) The flux splitting in the above two equations is known as the locally Lax–Friedrichs (LLF) flux splitting. Now, please focus on Figure 1. We see a mesh with zones, and zone boundaries, as well as a mesh function that is specified at zone centers. At each zone center, we can use the point value of the mesh function to also evaluate the zone-centered point value for the flux. These zone-centered flux values are to be used to obtain the numerical flux  $\hat{F}_{i+1/2}$  at the purple zone boundary in Figure 1. But realize that the numerical flux  $\hat{F}_{i+1/2}$  is constituted by the sum of  $\hat{F}_{i+1/2}^+$  (which carries the right-going flux contributions) and  $\hat{F}_{i+1/2}^-$  (which carries the left-going flux contributions). If  $\hat{F}_{i+1/2}^+$  and  $\hat{F}_{i+1/2}^-$  are obtained via a high-order, one-dimensional finite-volume-style reconstruction, then the entire scheme shown in Equation (19) will be high-order accurate in space. This paragraph has, therefore, shown how the flux splitting is to be used in FD-WENO schemes for conservation laws. Notice that in light of the discussion surrounding Equations (20), (21), and (22), the reconstruction has to be a finite-volume style reconstruction. In such a reconstruction, the zone averages are known, as shown in the right-hand side of Equation (22), and the reconstruction polynomial has to be constructed so as to match the zone averages.

The previous paragraph addressed the issue of flux splitting. But it did not address the twin issues of upwinding and nonlinear hybridization. We know that these two concepts are essential for obtaining a stable scheme. Upwinding requires that any stencils that contribute to the right-going flux  $\hat{F}_{i+1/2}^+$  must include the zone that is left of the zone boundary “ $i + 1/2$ .” As a result, those stencils must include zone “ $i$ ” in Figure 1. We see that this requirement is met by the stencils shown in Figure 1. Upwinding also requires that any stencils that

contribute to the left-going flux  $\hat{F}_{i+1/2}^-$  must include the zone that is right of the zone boundary “ $i + 1/2$ .” As a result, those stencils must include zone “ $i + 1$ ” in Figure 1, and we see that this requirement is met by the stencils shown in Figure 1.

Now that flux splitting and upwinding have been clarified, let us address the issue of nonlinear hybridization. Over the years, there have been many interpretations of what it means to nonlinearly hybridize the available stencils in a WENO scheme (G.-S. Jiang & C.-W. Shu 1996; D. S. Balsara & C.-W. Shu 2000; D. Levy et al. 2000; A. K. Henrick et al. 2006; R. Borges et al. 2008; D. S. Balsara et al. 2016; I. Cravero & M. Semplice 2016; J. Zhu & J. Qiu 2016; J. Zhu & C.-W. Shu 2018). Figure 1 shows the WENO-AO approach of D. S. Balsara et al. (2016), where “AO” stands for adaptive order. Figure 1 focuses on a fifth-order WENO-AO reconstruction, but the methods have been extended up to 11th order. The three smaller left-biased, zone-centered, and right-biased stencils cover the zones of interest, i.e., zone “ $i$ ” and zone “ $i + 1$ ,” respectively. Their nonlinear hybridization would give a stable stencil that is third-order accurate. For example, consider the stencils with the right arrow in Figure 1 that contribute to  $\hat{F}_{i+1/2}^+$ . The smaller stencils include the left-biased stencil, which includes zones  $\{i - 2, i - 1, i\}$ , the centered stencil, which includes zones  $\{i - 1, i, i + 1\}$ , and the right-biased stencil, which includes zones  $\{i, i + 1, i + 2\}$ . Together, these three smaller stencils, if they are nonlinearly hybridized among themselves, would yield a stable, spatially third-order accurate reconstruction over the zone “ $i$ ,” which must be included in the upwinding of  $\hat{F}_{i+1/2}^+$ . To get a fifth-order accurate reconstruction over the zone “ $i$ ,” one must make a nonlinear hybridization of these smaller stencils with the larger stencil in Figure 1, which includes zones  $\{i - 2, i - 1, i, i + 1, i + 2\}$ . The smaller stencils guarantee stability when stability becomes an issue. The larger stencil provides higher (fifth) order accuracy when the solution is

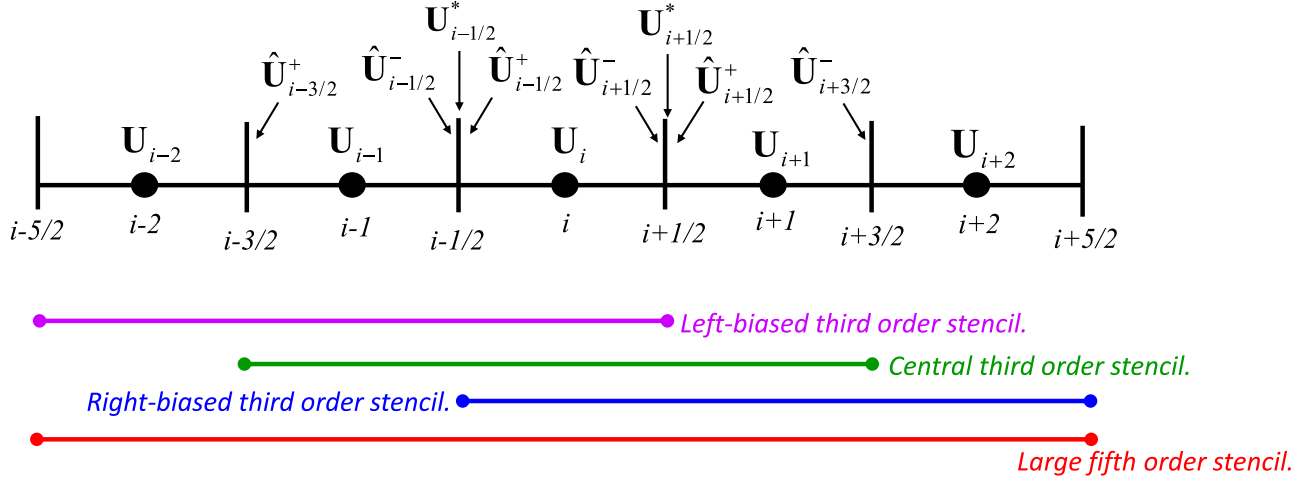


**Figure 2.** The panel shows part of the mesh around zone “ $i$ .” The mesh functions are collocated at the zone centers, as shown by the thick dots. The zone boundaries are shown by the vertical lines. The figure also shows the stencils associated with the zone “ $i$ ” for the fifth-order WENO-AO reconstruction/interpolation. We have three smaller third-order stencils and a large fifth-order stencil. The reconstructed/interpolated variables at the zone boundaries are shown with a caret. The variables with a superscript star are resolved states obtained by the pointwise application of a simple HLL or LLF Riemann solver at the zone boundaries.

smooth enough to justify the higher accuracy. The stencils for obtaining a fifth order in space approximation for the right-going flux are shown by the stencils with a right-pointing arrow in Figure 1. Figure 1 also displays the smaller and larger stencils used for the spatially fifth-order accurate, upwinded reconstruction of the left-going flux  $\hat{F}_{i+1/2}^-$ . The stencils for obtaining a fifth order in space approximation for the left-going flux are shown by the stencils with a left-pointing arrow in Figure 1. We can see that all those stencils in Figure 1 cover the zone “ $i+1$ .” The final FD-WENO scheme for conservation laws is then given by

$$\partial_t U_i = - \frac{(\hat{F}_{i+1/2}^+ + \hat{F}_{i+1/2}^-) - (\hat{F}_{i-1/2}^+ + \hat{F}_{i-1/2}^-)}{\Delta x}. \quad (25)$$

The reader can obtain further detail associated with WENO-AO reconstruction shown in Figure 1 from Sections 2 and 3 of D. S. Balsara et al. (2016). We should also mention that the reconstruction should be done in characteristic variables in order to obtain the best quality solution. This completes our very brief description of FD-WENO for conservation laws. This FD-WENO scheme for conservation laws will prove indispensable in the next section for understanding FD-WENO schemes for systems in nonconservation form like the FO-Z4 formulation of the Einstein equations.

### 3.2. FD-WENO Schemes for Hyperbolic Systems with Nonconservative Products

For a very long time, FD-WENO schemes were only available for conservation laws. However, first-order formulations of the Einstein equations, as are nowadays presented (J. D. Brown et al. 2012; M. Dumbser et al. 2018, 2024), are cast in a nonconservative form like Equation (16). Here, to simplify the description of the numerical scheme, we disregard the source terms on the right-hand side and we consider

$$\partial_t U + A(U) \partial_x U = 0 \iff \partial_t U = -A(U) \partial_x U. \quad (26)$$

Such situations are best handled in fluctuation form. The problem was that, until the advent of D. S. Balsara et al. (2023a), fluctuation form-based FD-WENO schemes were not available for Equation (26). Equation (16) in Section 4 of D. S. Balsara et al. (2023a) yields a scheme that can be applied to Equation (26). In Section 5 of D. S. Balsara et al. (2023a), we do provide a derivation of the scheme. However, that derivation is somewhat harder to understand, so we present a much simpler derivation here. We give this derivation in the limit of a linear flux,  $F = AU$ , with “ $A$ ” as a constant matrix, but the final form that we will obtain will be in fluctuation form so that it can be extended to include any Riemann solver that accommodates the nonlinearities at the zone boundaries. As in D. S. Balsara et al. (2023a), we work in the limit of the LLF flux.

Figure 2, where the solution vector has itself been reconstructed. Because we are only reconstructing the solution vector, only one reconstruction is needed within each zone. (This is different from what is shown in Figure 1, which uses two reconstructions for each of the right-going and left-going fluxes per zone.) As a result, at each zone boundary, say the zone boundary “ $i+1/2$ ” in Figure 2, we have the left state  $\hat{U}_{i+1/2}^-$  and the right state  $\hat{U}_{i+1/2}^+$ . Please try to understand how  $\hat{F}_{i+1/2}^-$  in Figure 1 relates to  $\hat{U}_{i+1/2}^+$  in Figure 2. Likewise, please try to understand how  $\hat{F}_{i+1/2}^+$  in Figure 1 relates to  $\hat{U}_{i+1/2}^-$  in Figure 2. With “ $A$ ” held constant, we first write

$$\begin{aligned} \hat{F}_{i+1/2}^- &= \frac{1}{2}(A - SI)\hat{U}_{i+1/2}^+; \\ \hat{F}_{i+1/2}^+ &= \frac{1}{2}(A + SI)\hat{U}_{i+1/2}^-; \\ \hat{F}_{i-1/2}^- &= \frac{1}{2}(A - SI)\hat{U}_{i-1/2}^+; \\ \hat{F}_{i-1/2}^+ &= \frac{1}{2}(A + SI)\hat{U}_{i-1/2}^-. \end{aligned} \quad (27)$$



It is then easy to show that

$$\begin{aligned}
 -(\hat{\mathbf{F}}_{i+1/2}^- + \hat{\mathbf{F}}_{i+1/2}^+) &= -\frac{1}{2}(\mathbf{A} - S\mathbf{I})\hat{\mathbf{U}}_{i+1/2}^+ \\
 &\quad - \frac{1}{2}(\mathbf{A} + S\mathbf{I})\hat{\mathbf{U}}_{i+1/2}^- \\
 &= -\frac{1}{2}(\mathbf{A} - S\mathbf{I})\hat{\mathbf{U}}_{i+1/2}^+ + \frac{1}{2}(\mathbf{A} - S\mathbf{I})\hat{\mathbf{U}}_{i+1/2}^- - \mathbf{A}\hat{\mathbf{U}}_{i+1/2}^- \\
 &= -\frac{1}{2}(\mathbf{A} - S\mathbf{I})(\hat{\mathbf{U}}_{i+1/2}^+ - \hat{\mathbf{U}}_{i+1/2}^-) - \mathbf{A}\hat{\mathbf{U}}_{i+1/2}^- \\
 &= -\mathbf{D}_{i+1/2}^- - \mathbf{A}\hat{\mathbf{U}}_{i+1/2}^-.
 \end{aligned} \tag{28}$$

It is also easy to show via a similar derivation that

$$\begin{aligned}
 (\hat{\mathbf{F}}_{i-1/2}^- + \hat{\mathbf{F}}_{i-1/2}^+) &= \frac{1}{2}(\mathbf{A} - S\mathbf{I})\hat{\mathbf{U}}_{i-1/2}^+ \\
 &\quad + \frac{1}{2}(\mathbf{A} + S\mathbf{I})\hat{\mathbf{U}}_{i-1/2}^- \\
 &= -\frac{1}{2}(\mathbf{A} + S\mathbf{I})\hat{\mathbf{U}}_{i-1/2}^+ + \frac{1}{2}(\mathbf{A} + S\mathbf{I})\hat{\mathbf{U}}_{i-1/2}^- + \mathbf{A}\hat{\mathbf{U}}_{i-1/2}^+ \\
 &= -\frac{1}{2}(\mathbf{A} + S\mathbf{I})(\hat{\mathbf{U}}_{i-1/2}^+ - \hat{\mathbf{U}}_{i-1/2}^-) + \mathbf{A}\hat{\mathbf{U}}_{i-1/2}^+ \\
 &= -\mathbf{D}_{i-1/2}^+ + \mathbf{A}\hat{\mathbf{U}}_{i-1/2}^+.
 \end{aligned} \tag{29}$$

In the above two equations, and for a linear system, we can define the left-going and right-going fluctuations as  $\mathbf{D}_{i+1/2}^- \equiv [(\mathbf{A} - S\mathbf{I})/2](\hat{\mathbf{U}}_{i+1/2}^+ - \hat{\mathbf{U}}_{i+1/2}^-)$  and  $\mathbf{D}_{i-1/2}^+ \equiv [(\mathbf{A} + S\mathbf{I})/2](\hat{\mathbf{U}}_{i-1/2}^+ - \hat{\mathbf{U}}_{i-1/2}^-)$ , respectively. We will soon point to references where their nonlinear extensions can be obtained. Putting the above two equations together, we can now show that

$$\begin{aligned}
 & - \frac{(\hat{\mathbf{F}}_{i+1/2}^+ + \hat{\mathbf{F}}_{i+1/2}^-) - (\hat{\mathbf{F}}_{i-1/2}^+ + \hat{\mathbf{F}}_{i-1/2}^-)}{\Delta x} \\
 &= -\frac{1}{\Delta x}(\mathbf{D}_{i+1/2}^- + \mathbf{D}_{i-1/2}^+) - \mathbf{A} \frac{(\hat{\mathbf{U}}_{i+1/2}^- - \hat{\mathbf{U}}_{i-1/2}^+)}{\Delta x}. \tag{30}
 \end{aligned}$$

While the above derivation was done in a simpler context, it is now easy to identify the fully updated equation:

$$\begin{aligned}
 \partial_t \mathbf{U}_i &= -\frac{1}{\Delta x}(\mathbf{D}_{\text{HLLI}}^-(\hat{\mathbf{U}}_{i+1/2}^-, \hat{\mathbf{U}}_{i+1/2}^+) + \mathbf{D}_{\text{HLLI}}^+(\hat{\mathbf{U}}_{i-1/2}^-, \hat{\mathbf{U}}_{i-1/2}^+)) \\
 &\quad \times (\hat{\mathbf{U}}_{i-1/2}^-, \hat{\mathbf{U}}_{i-1/2}^+) - \mathbf{A}(\mathbf{U}_i) \frac{(\hat{\mathbf{U}}_{i+1/2}^- - \hat{\mathbf{U}}_{i-1/2}^+)}{\Delta x}. \tag{31}
 \end{aligned}$$

The fluctuation  $\mathbf{D}_{\text{HLLI}}^-(\hat{\mathbf{U}}_{i+1/2}^-, \hat{\mathbf{U}}_{i+1/2}^+)$  captures the contribution from the left-going waves at zone boundary “ $i + 1/2$ .” The fluctuation  $\mathbf{D}_{\text{HLLI}}^+(\hat{\mathbf{U}}_{i-1/2}^-, \hat{\mathbf{U}}_{i-1/2}^+)$  captures the contribution from the right-going waves at zone boundary “ $i - 1/2$ .” The subscript “HLLI” indicates that we are using the HLLI Riemann solver from M. Dumbser & D. S. Balsara (2016), which can indeed handle nonlinearities in PDE systems of the form shown in Equation (26). Appendix C of M. Dumbser &

D. S. Balsara (2016) provides further details on evaluating fluctuations for PDEs with nonlinearities.

In the previous subsection we have mentioned that it is advantageous to carry out the reconstruction in the characteristic variables. In a tour de force, the 54 eigenvectors of the FO-Z4 system for the full Einstein–Euler system have been derived in M. Dumbser et al. (2024). However, it would be prohibitive to project the entire system into that eigenspace for carrying out a reconstruction of the solution vector. Fortunately, the eigenspace splits into a five-component subspace for the hydrodynamic system and an eigenspace for the rest of the system. We recall that, although no physical shocks can form in the metric since all the spacetime fields are linearly degenerate, gauge shocks can still form as a result of the gauge conditions chosen (M. Alcubierre 2003; E. Jiménez-Vázquez & M. Alcubierre 2022; T. W. Baumgarte et al. 2023a, 2023b). In this respect, it could be quite beneficial to treat the reconstruction of the variables in the GR sector using characteristic projection. However, due to the complexity of the equations, we have not followed this approach here and we postpone the analysis of such a specialized aspect to a future investigation.

It is also useful to observe that Equation (31) is not in exact flux conservative form. An exact flux conservative form is essential (because of the Lax–Wendroff theorem) for accurately predicting shock locations when the system is conservative, as is the case for hydrodynamics. The modern trend is to seek out schemes that revert to a conservation form when such is present. However, Equation (31) does derive from Equation (25), which is in conservation form, so for most practical cases, it does a rather good job of predicting shock locations. Besides, since the solutions of the Einstein equations are continuous in the metric terms, except of course when a

singularity forms or when gauge shocks are present, the lack of a conservation form is not a major impediment. As a result, Equation (31) has an important place in the solution of the Einstein equations. This completes our description of FD-WENO schemes as they are extended to hyperbolic PDEs, like the FO-Z4 system, that are not in conservation form.

### 3.3. AFD-WENO Schemes for Conservation Laws

The previous subsection has shown us how to obtain a scheme that is fully in nonconservative form. It is very easy to implement and very suitable for the Einstein equations in vacuum, i.e., when evolving the hydrodynamics is not a priority. However, it is often the case that one has to simultaneously evolve the equations for relativistic hydrodynamics in addition to the Einstein equations. In that case, we will need a scheme that can handle nonconservative products and is, nevertheless, versatile enough to revert to a conservation form when such a conservation form is present in the problem. The scheme in the previous subsection does not meet this requirement. We have also seen that a study of conservation laws is a first step toward deriving methods that can handle nonconservative products. Therefore, in this subsection, we will present an AFD-WENO scheme for conservation laws. This will be an essential first step toward deriving schemes that can seamlessly accommodate both a conservation law as well as nonconservative products—that will be the task of the next section.

This and the next subsection rely on interpolation, which is different from the reconstruction that was used in the previous two subsections. It is, therefore, worthwhile to make a distinction between reconstruction and interpolation. Reconstruction is used in all finite-volume astrophysical codes and also in the previous FD-WENO schemes where the fluxes or states are reconstructed. It consists of starting with the zone averages in a given stencil and obtaining therefrom the high degree polynomial whose integration over each of the zones of the stencil matches the original zone averages. Interpolation is used less often in the numerical solution of conservation laws; however, it is the approach that will be needed in this and the next subsection. It consists of starting with the point values at each of the zone centers of a stencil and obtaining therefrom the high degree polynomial that matches those point values. Therefore, the two words, reconstruction and interpolation, carry different connotations. When applied to the same stencil, reconstruction, and interpolation produce polynomials with the same degree. However, the underlying polynomial coefficients that are produced by invoking reconstruction or interpolation on a given stencil can indeed be very different. Standard WENO concepts like linear weights, smoothness indicators, normalized nonlinear weights, etc. are often the same for reconstruction and interpolation. So there is indeed a beneficial transference of knowledge between them. WENO reconstruction, especially as it relates to FD-WENO schemes, has been amply documented in the literature starting from G.-S. Jiang & C.-W. Shu (1996), D. S. Balsara & C.-W. Shu (2000) and continuing through D. S. Balsara et al. (2016), where it was presented in its most polished form. The WENO interpolation, as it relates to AFD-WENO, has also been recently documented in a very polished form in Sections 3 and 4 of D. S. Balsara et al. (2024a).

Let us say that we have a high-order pointwise WENO interpolation strategy that is applied to the solution vector of the mesh. At each zone boundary, say “ $i + 1/2$ ,” we will then

have high-order interpolants  $\hat{U}_{i+1/2}^-$  and  $\hat{U}_{i+1/2}^+$ . Figure 2 shows us that the same stencils can be used for interpolation and reconstruction. Say also that we invoke the Riemann solver (in pointwise fashion) at each zone boundary to obtain  $F^*(\hat{U}_{i+1/2}^-, \hat{U}_{i+1/2}^+)$ . The flux from the previous sentence will indeed be a suitably high-order flux at the zone boundary “ $i + 1/2$ .” However, say that we naively assert a discrete in space but continuous in time update in the zone “ $i$ ” of the form

$$\partial_t U_i = -\frac{1}{\Delta x} (F^*(\hat{U}_{i+1/2}^-, \hat{U}_{i+1/2}^+) - F^*(\hat{U}_{i-1/2}^-, \hat{U}_{i-1/2}^+)). \quad (32)$$

We would find, to our chagrin, that Equation (32) only has second-order spatial accuracy. Even if the solution had been very smooth, and even if the interpolation had been carried out with very high-order accuracy, the above equation would only result in a spatially second-order scheme. Understanding why this is so will indeed show us the way out of this dilemma. We illustrate this for the simplest case, where we assume that we are trying to obtain a third-order accurate scheme. Because we have assumed a very smooth solution and a very smooth flux, we can make the Taylor series expansion

$$F(x) = f_0 + x(\partial_x f)_0 + \frac{x^2}{2}(\partial_x^2 f)_0 + \frac{x^3}{6}(\partial_x^3 f)_0 + \dots \quad (33)$$

All the terms of the Taylor series,  $f_0$ ,  $(\partial_x f)_0$ ,  $(\partial_x^2 f)_0$ ,  $(\partial_x^3 f)_0$  are all evaluated at  $x = 0$ . We can evaluate Equation (33) and its higher derivatives at  $x = \pm \Delta x/2$  to get

$$\begin{aligned} F(x)|_{x=\pm\Delta x/2} &= f_0 \pm \frac{\Delta x}{2}(\partial_x f)_0 \\ &\quad + \frac{\Delta x^2}{8}(\partial_x^2 f)_0 \pm \frac{\Delta x^3}{48}(\partial_x^3 f)_0 + \dots; \\ \partial_x F(x)|_{x=\pm\Delta x/2} &= (\partial_x f)_0 \pm \frac{\Delta x}{2}(\partial_x^2 f)_0 \\ &\quad + \frac{\Delta x^2}{8}(\partial_x^3 f)_0 \pm \dots; \\ \partial_x^2 F(x)|_{x=\pm\Delta x/2} &= (\partial_x^2 f)_0 \pm \frac{\Delta x}{2}(\partial_x^3 f)_0 + \dots \end{aligned} \quad (34)$$

Finite differencing the point values of the fluxes at  $x = \pm \Delta x/2$  gives

$$\begin{aligned} \frac{1}{\Delta x} [F(x)|_{x=\Delta x/2} - F(x)|_{x=-\Delta x/2}] \\ = (\partial_x f)_0 + \frac{\Delta x^2}{24}(\partial_x^3 f)_0. \end{aligned} \quad (35)$$

The error term, which is proportional to  $\Delta x^2$  in Equation (35), tells us that the scheme is only second-order accurate regardless of the accuracy of the interpolation. Now realize that if this were a good  $k$ th-order scheme, it should have returned  $(\partial_x f)_0$  at  $x = 0$  with an error term that is proportional to  $\Delta x^k$ . That is indeed the true meaning of finite differencing the right-hand side of Equation (18). Instead, the presence of  $\Delta x^2(\partial_x^3 f)_0/24$  prevents Equation (35) from even being a third-order accurate expression. However, realize that a third derivative at the zone center is equivalent to finite differencing two second derivatives that are evaluated at the zone boundaries. Thus,

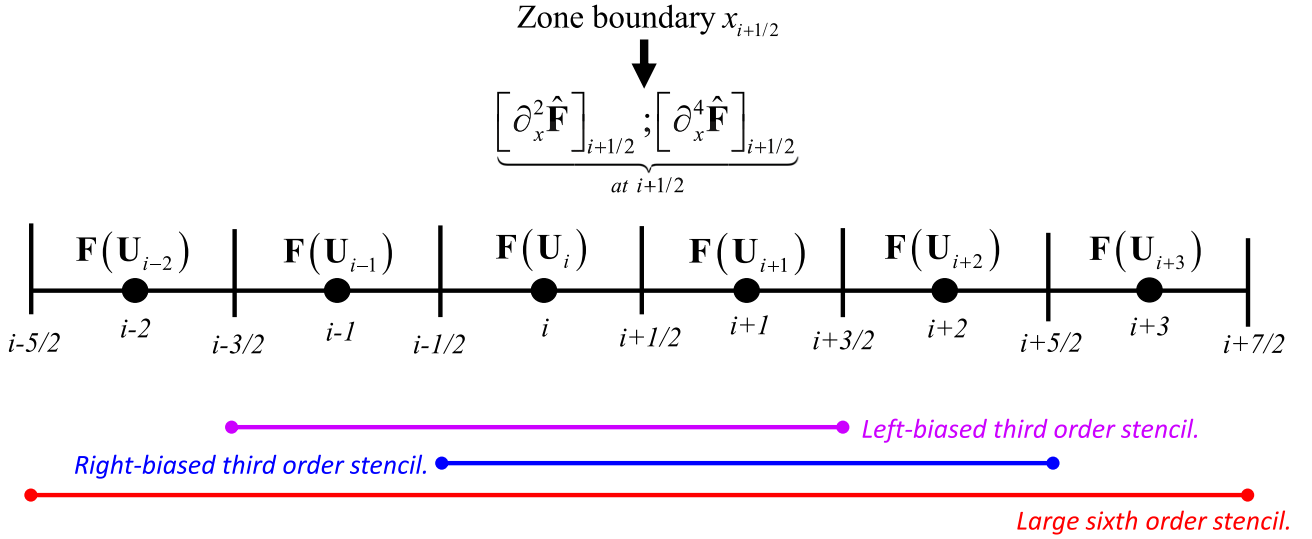


**Figure 3.** The panel shows part of the mesh around the zone boundary “ $i + 1/2$ .” The fluxes are evaluated pointwise at the zone centers, as shown by the thick dots. The zone boundaries are shown by the vertical lines. The figure also shows the stencils associated with the zone boundary “ $i + 1/2$ ” for the third and fifth-order AFD-WENO schemes. We have two smaller third-order stencils and a large sixth-order stencil. For a third-order AFD-WENO scheme, the two smaller stencils can be nonlinearly hybridized. In that case, the second derivatives of the flux can be obtained at the zone boundary when the smoothness in the solution warrants it. For fifth-order AFD-WENO, the two smaller stencils can be nonlinearly hybridized along with the larger stencil. In that case, the second and fourth derivatives of the flux can be obtained at the zone boundary when the smoothness in the solution warrants it. The process described here can be done for AO and multiresolution WENO interpolation.

we can take our numerical fluxes at  $x = \pm \Delta x/2$  to be

$$\mathbf{F}_{x=\pm\Delta x/2}^{\text{num}} = [\mathbf{F}(x)]_{x=\pm\Delta x/2} - \frac{\Delta x^2}{24} [\partial_x^2 \mathbf{F}(x)]_{x=\pm\Delta x/2}. \quad (36)$$

By finite differencing the numerical fluxes from Equation (36) we can easily see that

$$\frac{1}{\Delta x} [\mathbf{F}_{x=\Delta x/2}^{\text{num}} - \mathbf{F}_{x=-\Delta x/2}^{\text{num}}] = (\partial_x \mathbf{f})_0 + O(\Delta x^4). \quad (37)$$

In other words, the correction term in Equation (36) with the higher-order flux derivative was essential for restoring accuracy.

Appendix A of D. S. Balsara et al. (2024a) shows us how to design an AFD-WENO scheme for conservation laws up to any desired accuracy. For up to ninth-order of accuracy, the resulting AFD-WENO scheme is explicitly given by

third-order scheme. In that case, the second derivatives of  $\mathbf{F}$  have to be evaluated at the zone boundaries with a WENO interpolation scheme that is at least third-order accurate. If the red terms are also included, in addition to the black terms, the scheme becomes fifth-order accurate. In that case, all the derivatives of  $\mathbf{F}$  have to be evaluated at the zone boundaries with a WENO interpolation scheme that is at least fifth-order accurate. If the blue terms are also included, in addition to the black and red terms, we get a seventh-order scheme. In that case, all the derivatives of  $\mathbf{F}$  have to be evaluated at the zone boundaries with a WENO interpolation scheme that is at least seventh-order accurate. If the magenta terms are included, in addition to the black, red, and blue terms, we get a ninth-order scheme. In that case, all the derivatives of  $\mathbf{F}$  have to be evaluated at the zone boundaries with a WENO interpolation scheme that is at least ninth-order accurate. The WENO-based process by which these higher-order derivatives can be

$$\begin{aligned} \partial_t \mathbf{U}_i = & -\frac{1}{\Delta x} \{ \mathbf{F}^*(\hat{\mathbf{U}}_{i+1/2}^-, \hat{\mathbf{U}}_{i+1/2}^+) - \mathbf{F}^*(\hat{\mathbf{U}}_{i-1/2}^-, \hat{\mathbf{U}}_{i-1/2}^+) \} \\ & - \frac{1}{\Delta x} \left\{ \left[ -\frac{1}{24} (\Delta x)^2 [\partial_x^2 \mathbf{F}]_{i+1/2} + \frac{7}{5760} (\Delta x)^4 [\partial_x^4 \mathbf{F}]_{i+1/2} \right. \right. \\ & - \frac{31}{967,680} (\Delta x)^6 [\partial_x^6 \mathbf{F}]_{i+1/2} + \frac{127}{154,828,800} (\Delta x)^8 [\partial_x^8 \mathbf{F}]_{i+1/2} \left. \right] \\ & - \left[ -\frac{1}{24} (\Delta x)^2 [\partial_x^2 \mathbf{F}]_{i-1/2} + \frac{7}{5760} (\Delta x)^4 [\partial_x^4 \mathbf{F}]_{i-1/2} \right. \\ & \left. \left. - \frac{31}{967,680} (\Delta x)^6 [\partial_x^6 \mathbf{F}]_{i-1/2} + \frac{127}{154,828,800} (\Delta x)^8 [\partial_x^8 \mathbf{F}]_{i-1/2} \right] \right\}. \end{aligned} \quad (38)$$

Notice that Equation (38) is still in conservation form, and therefore, it should be able to capture shock locations accurately. The black terms in the above equation yield a

obtained without engendering any Gibbs phenomenon is described in Section 4 of D. S. Balsara et al. (2024a). The stencils that are used within a fifth-order scheme to obtain the



higher-order flux derivatives at the zone boundaries are also shown schematically in Figure 3 of this paper. This completes our discussion of AFD-WENO schemes for conservation laws.

### 3.4. AFD-WENO Schemes for Hyperbolic Systems with Nonconservative Products

The key purpose of the previous section was to lead us to the AFD-WENO schemes for hyperbolic systems with some flux terms and some nonconservative products. Since first-order treatments of GR produce hyperbolic systems that are of this type, such AFD-WENO schemes are most useful for GR. Such schemes have been obtained very recently by D. S. Balsara et al. (2024b) and we briefly show the reader why they work in this subsection. In one dimension, such systems can be formally written as

$$\partial_t \mathbf{U} + \partial_x \mathbf{F}(\mathbf{U}) + \mathbf{C}(\mathbf{U}) \partial_x \mathbf{U} = 0. \quad (39)$$

Here,  $\mathbf{C}(\mathbf{U})$  is a solution-dependent matrix of nonconservative products.

The trick for the derivation is to start with a conservation law of the same form as Equation (18) but to rewrite it differently as

$$\begin{aligned} \partial_t \mathbf{U} + \partial_x \mathbf{F}(\mathbf{U}) &= 0 \quad \text{with the flux splitting} \\ \mathbf{F}(\mathbf{U}) &= \mathbf{F}_C(\mathbf{U}) + \mathbf{F}_{NC}(\mathbf{U}). \end{aligned} \quad (40)$$

In other words, we will be effecting a trompe l'oeil where we will treat the flux  $\mathbf{F}_C(\mathbf{U})$  in conservation form but we will write  $\mathbf{F}_{NC}(\mathbf{U})$  as if it can only be written as a nonconservative product. The Jacobians of the fluxes can now be written as

$$\begin{aligned} \mathbf{A}(\mathbf{U}) &= \frac{\partial(\mathbf{F}_C(\mathbf{U}) + \mathbf{F}_{NC}(\mathbf{U}))}{\partial \mathbf{U}} = \mathbf{B}(\mathbf{U}) + \mathbf{C}(\mathbf{U}) \quad \text{with} \\ \mathbf{B}(\mathbf{U}) &\equiv \frac{\partial \mathbf{F}_C(\mathbf{U})}{\partial \mathbf{U}} \quad \text{and} \quad \mathbf{C}(\mathbf{U}) \equiv \frac{\partial \mathbf{F}_{NC}(\mathbf{U})}{\partial \mathbf{U}}. \end{aligned} \quad (41)$$

The upshot is that Equation (40) can now be written in the following equivalent forms:

$$\begin{aligned} \partial_t \mathbf{U} + \partial_x \mathbf{F}(\mathbf{U}) &= 0 \\ \Leftrightarrow \partial_t \mathbf{U} + \mathbf{A}(\mathbf{U}) \partial_x \mathbf{U} &= 0 \\ \Leftrightarrow \partial_t \mathbf{U} + \partial_x \mathbf{F}_C(\mathbf{U}) + \mathbf{C}(\mathbf{U}) \partial_x \mathbf{U} &= 0. \end{aligned} \quad (42)$$

It is now easy to see that if we initially obtain a scheme for the rightmost equation in Equation (42), then we can eventually obtain a scheme for Equation (39) just by dropping the subscript “C” in  $\mathbf{F}_C(\mathbf{U})$ .

We start our derivation by writing the resolved fluxes  $\mathbf{F}^*(\hat{\mathbf{U}}_{i+1/2}^-, \hat{\mathbf{U}}_{i+1/2}^+)$  and  $\mathbf{F}^*(\hat{\mathbf{U}}_{i-1/2}^-, \hat{\mathbf{U}}_{i-1/2}^+)$  in the form of fluctuations by using the following definitions for the left-going and right-going fluctuations:

$$\begin{aligned} \mathbf{F}^*(\hat{\mathbf{U}}_{i+1/2}^-, \hat{\mathbf{U}}_{i+1/2}^+) &= \mathbf{D}^{*-}(\hat{\mathbf{U}}_{i+1/2}^-, \hat{\mathbf{U}}_{i+1/2}^+) \\ &\quad + \mathbf{F}_C(\hat{\mathbf{U}}_{i+1/2}^-) + \mathbf{F}_{NC}(\hat{\mathbf{U}}_{i+1/2}^+); \\ \mathbf{F}^*(\hat{\mathbf{U}}_{i-1/2}^-, \hat{\mathbf{U}}_{i-1/2}^+) &= -\mathbf{D}^{*+}(\hat{\mathbf{U}}_{i-1/2}^-, \hat{\mathbf{U}}_{i-1/2}^+) \\ &\quad + \mathbf{F}_C(\hat{\mathbf{U}}_{i-1/2}^+) + \mathbf{F}_{NC}(\hat{\mathbf{U}}_{i-1/2}^-). \end{aligned} \quad (43)$$

Putting Equation (43) in Equation (38) allows us to write the intermediate equation:

$$\begin{aligned} \partial_t \mathbf{U}_i &= -\frac{1}{\Delta x} \{ \mathbf{D}^{*-}(\hat{\mathbf{U}}_{i+1/2}^-, \hat{\mathbf{U}}_{i+1/2}^+) + \mathbf{D}^{*+}(\hat{\mathbf{U}}_{i-1/2}^-, \hat{\mathbf{U}}_{i-1/2}^+) \} \\ &\quad - \frac{1}{\Delta x} \{ \mathbf{F}_C(\hat{\mathbf{U}}_{i+1/2}^-) - \mathbf{F}_C(\hat{\mathbf{U}}_{i-1/2}^+) \} \\ &\quad - \frac{1}{\Delta x} \{ \mathbf{F}_{NC}(\hat{\mathbf{U}}_{i+1/2}^-) - \mathbf{F}_{NC}(\hat{\mathbf{U}}_{i-1/2}^+) \} \\ &\quad - \frac{1}{\Delta x} \left\{ \left[ -\frac{1}{24} (\Delta x)^2 [\partial_x^2 \mathbf{F}]_{i+1/2} \right. \right. \\ &\quad + \frac{7}{5760} (\Delta x)^4 [\partial_x^4 \mathbf{F}]_{i+1/2} \\ &\quad - \frac{31}{967,680} (\Delta x)^6 [\partial_x^6 \mathbf{F}]_{i+1/2} \\ &\quad + \frac{127}{154,828,800} (\Delta x)^8 [\partial_x^8 \mathbf{F}]_{i+1/2} \Big] \\ &\quad - \left[ -\frac{1}{24} (\Delta x)^2 [\partial_x^2 \mathbf{F}]_{i-1/2} \right. \\ &\quad + \frac{7}{5760} (\Delta x)^4 [\partial_x^4 \mathbf{F}]_{i-1/2} \\ &\quad - \frac{31}{967,680} (\Delta x)^6 [\partial_x^6 \mathbf{F}]_{i-1/2} \\ &\quad \left. \left. + \frac{127}{154,828,800} (\Delta x)^8 [\partial_x^8 \mathbf{F}]_{i-1/2} \right] \right\}. \end{aligned} \quad (44)$$

Now, we will write the term  $\{\mathbf{F}_{NC}(\hat{\mathbf{U}}_{i+1/2}^-) - \mathbf{F}_{NC}(\hat{\mathbf{U}}_{i-1/2}^+)\}$  as a term that looks like  $\mathbf{C}(\mathbf{U}_i)(\partial_x \hat{\mathbf{U}})_i$  along with some higher-order terms which will eventually cancel off. We write

$$\begin{aligned} &-\frac{1}{\Delta x} \{ \mathbf{F}_{NC}(\hat{\mathbf{U}}_{i+1/2}^-) - \mathbf{F}_{NC}(\hat{\mathbf{U}}_{i-1/2}^+) \} \\ &\quad \cong -(\partial_x \mathbf{F}_{NC})_i - \left\{ + \frac{\Delta x^2}{24} (\partial_x^3 \mathbf{F}_{NC})_i + \frac{\Delta x^4}{1920} (\partial_x^5 \mathbf{F}_{NC})_i \right. \\ &\quad \left. + \frac{\Delta x^6}{322,560} (\partial_x^7 \mathbf{F}_{NC})_i + \frac{\Delta x^8}{92,897,280} (\partial_x^9 \mathbf{F}_{NC})_i \right\} \\ &\quad \cong -\mathbf{C}(\mathbf{U}_i)(\partial_x \hat{\mathbf{U}})_i - \frac{1}{\Delta x} \left\{ \left[ \frac{1}{24} (\Delta x)^2 [\partial_x^2 \mathbf{F}_{NC}]_{i+1/2} \right. \right. \\ &\quad - \frac{7}{5760} (\Delta x)^4 [\partial_x^4 \mathbf{F}_{NC}]_{i+1/2} \\ &\quad + \frac{31}{967,680} (\Delta x)^6 [\partial_x^6 \mathbf{F}_{NC}]_{i+1/2} \\ &\quad - \frac{127}{154,828,800} (\Delta x)^8 [\partial_x^8 \mathbf{F}_{NC}]_{i+1/2} \Big] \\ &\quad - \left[ \frac{1}{24} (\Delta x)^2 [\partial_x^2 \mathbf{F}_{NC}]_{i-1/2} - \frac{7}{5760} (\Delta x)^4 [\partial_x^4 \mathbf{F}_{NC}]_{i-1/2} \right. \\ &\quad + \frac{31}{967,680} (\Delta x)^6 [\partial_x^6 \mathbf{F}_{NC}]_{i-1/2} \\ &\quad \left. \left. - \frac{127}{154,828,800} (\Delta x)^8 [\partial_x^8 \mathbf{F}_{NC}]_{i-1/2} \right] \right\}. \end{aligned} \quad (45)$$

We insert Equation (45) in Equation (44) and use the fact that  $F_C(U) = F(U) - F_{NC}(U)$  to get the penultimate form of our updated equation:

$$\begin{aligned} \partial_t U_i = & -\frac{1}{\Delta x} \{D^{*-}(\hat{U}_{i+1/2}^-, \hat{U}_{i+1/2}^+) + D^{*+}(\hat{U}_{i-1/2}^-, \hat{U}_{i-1/2}^+)\} \\ & - \frac{1}{\Delta x} \{F_C(\hat{U}_{i+1/2}^-) - F_C(\hat{U}_{i-1/2}^+)\} - C(U_i)(\partial_x \hat{U})_i \\ & - \frac{1}{\Delta x} \left\{ \left[ -\frac{1}{24}(\Delta x)^2 [\partial_x^2 F_C]_{i+1/2} \right. \right. \\ & + \frac{7}{5760}(\Delta x)^4 [\partial_x^4 F_C]_{i+1/2} \\ & - \frac{31}{967,680}(\Delta x)^6 [\partial_x^6 F_C]_{i+1/2} \\ & \left. \left. + \frac{127}{154,828,800}(\Delta x)^8 [\partial_x^8 F_C]_{i+1/2} \right] \right. \\ & - \left[ -\frac{1}{24}(\Delta x)^2 [\partial_x^2 F_C]_{i-1/2} \right. \\ & + \frac{7}{5760}(\Delta x)^4 [\partial_x^4 F_C]_{i-1/2} \\ & - \frac{31}{967,680}(\Delta x)^6 [\partial_x^6 F_C]_{i-1/2} \\ & \left. \left. + \frac{127}{154,828,800}(\Delta x)^8 [\partial_x^8 F_C]_{i-1/2} \right] \right\}. \end{aligned} \quad (46)$$

Next, we will derive the final forms of the equations that we need.

The above equation would give us the update strategy for the last equation in Equation (42). But we want to transition from the last equation in Equation (42) to Equation (40). This is easily accomplished by dropping the subscript “C” in  $F_C(U)$  in Equation (46) to get one of our final equations as

$$\begin{aligned} \partial_t U_i = & -\frac{1}{\Delta x} \{D^{*-}(\hat{U}_{i+1/2}^-, \hat{U}_{i+1/2}^+) + D^{*+}(\hat{U}_{i-1/2}^-, \hat{U}_{i-1/2}^+)\} \\ & - \frac{1}{\Delta x} \{F(\hat{U}_{i+1/2}^-) - F(\hat{U}_{i-1/2}^+)\} - C(U_i)(\partial_x \hat{U})_i \\ & - \frac{1}{\Delta x} \left\{ \left[ -\frac{1}{24}(\Delta x)^2 [\partial_x^2 F]_{i+1/2} \right. \right. \\ & + \frac{7}{5760}(\Delta x)^4 [\partial_x^4 F]_{i+1/2} \\ & - \frac{31}{967,680}(\Delta x)^6 [\partial_x^6 F]_{i+1/2} \\ & \left. \left. + \frac{127}{154,828,800}(\Delta x)^8 [\partial_x^8 F]_{i+1/2} \right] \right. \\ & - \left[ -\frac{1}{24}(\Delta x)^2 [\partial_x^2 F]_{i-1/2} \right. \\ & + \frac{7}{5760}(\Delta x)^4 [\partial_x^4 F]_{i-1/2} \\ & - \frac{31}{967,680}(\Delta x)^6 [\partial_x^6 F]_{i-1/2} \\ & \left. \left. + \frac{127}{154,828,800}(\Delta x)^8 [\partial_x^8 F]_{i-1/2} \right] \right\}. \end{aligned} \quad (47)$$

The above equation is very illustrative. Notice that when the fluxes are absent, i.e., when the entire system is represented by the nonconservative products, the above equation reduces to

$$\begin{aligned} \partial_t U_i = & -\frac{1}{\Delta x} \{D^{*-}(\hat{U}_{i+1/2}^-, \hat{U}_{i+1/2}^+) \\ & + D^{*+}(\hat{U}_{i-1/2}^-, \hat{U}_{i-1/2}^+)\} - C(U_i)(\partial_x \hat{U})_i \end{aligned} \quad (48)$$

which is almost identical to Equation (31). (Recall that  $C(U_i) \rightarrow A(U_i)$  in that limit.) In other words, when solving just the Einstein equations, without additional hydrodynamic equations, AFD-WENO and FD-WENO become practically identical to one another. Of course, Equation (31) relies on reconstruction, whereas Equation (48) relies on interpolation. A form that is completely equivalent to Equation (47) at the analytical level, but has slightly better stability properties, can be written as

$$\begin{aligned} \partial_t U_i = & -\frac{1}{\Delta x} \{D_{i+1/2}^{*-}(\hat{U}_{i+1/2}^-, \hat{U}_{i+1/2}^+) + D_{i-1/2}^{*+} \\ & \times (\hat{U}_{i-1/2}^-, \hat{U}_{i-1/2}^+)\} - \frac{1}{\Delta x} \{F(\hat{U}_{i+1/2}^-) - F(\hat{U}_{i-1/2}^+)\} \\ & - \frac{1}{\Delta x} C(U_i)(\hat{U}_{i+1/2}^- - \hat{U}_{i-1/2}^+) - \frac{1}{\Delta x} C(U_i) \\ & \times \left\{ \left[ -\frac{1}{24}(\Delta x)^2 [\partial_x^2 \hat{U}]_{i+1/2} + \frac{7}{5760}(\Delta x)^4 [\partial_x^4 \hat{U}]_{i+1/2} \right. \right. \\ & - \frac{31}{967,680}(\Delta x)^6 [\partial_x^6 \hat{U}]_{i+1/2} + \frac{127}{154,828,800}(\Delta x)^8 [\partial_x^8 \hat{U}]_{i+1/2} \left. \right] \\ & - \left[ -\frac{1}{24}(\Delta x)^2 [\partial_x^2 \hat{U}]_{i-1/2} + \frac{7}{5760}(\Delta x)^4 [\partial_x^4 \hat{U}]_{i-1/2} \right. \\ & - \frac{31}{967,680}(\Delta x)^6 [\partial_x^6 \hat{U}]_{i-1/2} + \frac{127}{154,828,800}(\Delta x)^8 [\partial_x^8 \hat{U}]_{i-1/2} \left. \right] \left. \right\} \\ & - \frac{1}{\Delta x} \left\{ \left[ -\frac{1}{24}(\Delta x)^2 [\partial_x^2 F]_{i+1/2} + \frac{7}{5760}(\Delta x)^4 [\partial_x^4 F]_{i+1/2} \right. \right. \\ & - \frac{31}{967,680}(\Delta x)^6 [\partial_x^6 F]_{i+1/2} + \frac{127}{154,828,800}(\Delta x)^8 [\partial_x^8 F]_{i+1/2} \left. \right] \\ & - \left[ -\frac{1}{24}(\Delta x)^2 [\partial_x^2 F]_{i-1/2} + \frac{7}{5760}(\Delta x)^4 [\partial_x^4 F]_{i-1/2} \right. \\ & - \frac{31}{967,680}(\Delta x)^6 [\partial_x^6 F]_{i-1/2} + \frac{127}{154,828,800}(\Delta x)^8 [\partial_x^8 F]_{i-1/2} \left. \right] \left. \right\}. \end{aligned} \quad (49)$$

This completes our derivation of AFD-WENO schemes for systems with nonconservative products as they arise in GR. Along with the derivations, we have striven to provide insights into the strength of each scheme and its suitability for NR. Notice that the evaluation of the flux derivatives in Equations (47) or (49) is the same as was sketched in Figure 3. The evaluation of the higher derivatives of the states at the zone boundaries in Equation (49) also follows a process that is practically identical to Figure 3 and is described in detail in D. S. Balsara et al. (2024b).

Some overarching comments that connect the multiple FD-WENO formulations are in order.

1. Realize that the scheme in Section 3.1 relies on a flux splitting into an LLF flux and can, therefore, be somewhat dissipative. The schemes described in Sections 3.2, 3.3, and 3.4 can use improved Riemann solvers. Any good Riemann solver can be used in the schemes described in those three subsections. The HLLI

Riemann solver from M. Dumbser & D. S. Balsara (2016) might be very beneficial because it can handle all different types of intermediate waves including the contact discontinuities that are needed in well-balancing of hydrodynamic problems.

2. The AFD-WENO scheme in this subsection has an advantage over the FD-WENO scheme in Section 3.2 in that it recovers the conservation form when such a form is present. This can be very useful if the hydrodynamical equations are to be evolved in conjunction with the Einstein equations.
3. The term  $(\partial_x \hat{U})_i$  in Equation (47) has to be evaluated using the same WENO interpolation that was used for the state vector; as a result, Equation (47) usually shows one lower order of accuracy compared to Equation (49). Equation (47) may have some advantages for GR, nevertheless, because when the solution is smooth, it gives very good quality solutions at a lower computational cost.
4. When strong shocks are present, Equation (49) has slightly better stability properties compared to Equation (47) because the term  $C(U_i)(\hat{U}_{i+1/2}^- - \hat{U}_{i-1/2}^+)$  is itself treated in an FD form. However, since strong shocks are only present in the hydrodynamic sector in an NR calculation, the treatment of flux terms is identical in both equations.
5. We have only addressed spatial accuracy in this section. Like all FD-WENO schemes, the schemes presented here are to be coupled with strong stability preserving Runge–Kutta (SSP-RK) time stepping. Temporally high-order SSP-RK time stepping has been described in C.-W. Shu & S. Osher (1988) and R. J. Spiteri & S. J. Ruuth (2002, 2003).
6. In general, the treatment of the source terms in GR is such that the source terms are always non-stiff. As a result, we should not need variants of SSP-RK time stepping that include stiff source terms.
7. It would be useful to keep an eye on the ecosystem of ideas that are emerging around AFD-WENO methods. Such ideas include well-balancing, physical realizability, and preservation of divergence and curl constraints. These enhancements retain the low cost of the original AFD-WENO scheme.

This completes our discussion of FD-WENO and AFD-WENO schemes for systems with nonconservative products as they arise in GR.

### 3.5. Well-balancing of FD-WENO and AFD-WENO Schemes

Preserving the stationarity of an equilibrium solution  $U_e$  is far from trivial, and unless suitable steps are undertaken, a general numerical scheme will not be able to satisfy the condition  $\partial_t U_e = 0$  exactly over arbitrarily long timescales. This is particularly frustrating, for instance, if one is interested in studying numerically the oscillation modes of astrophysical objects in equilibrium. In these circumstances, if the order of magnitude of the discretization errors introduced by the numerical scheme is close to those of the physical initial perturbation under investigation, it will be impossible to distinguish between a physical effect and a numerical artifact. In the worst cases, the accumulation of numerical errors can even spoil completely the equilibrium solution over sufficiently

long timescales. Hence, a whole field of research exists to ensure the so-called *well-balancing* of a numerical scheme. Initially proposed in the context of the shallow water equations, well-balanced numerical schemes have been proposed in a variety of different techniques, sometimes tailored to specific PDE systems (A. Bermudez & M. Vázquez-Cendón 1994; R. J. LeVeque 1998; L. Gosse 2001; E. Audusse et al. 2004; N. Botta et al. 2004; M. J. Castro et al. 2017; M. J. Castro & C. Pares 2020; E. Gaburro et al. 2021; D. Bhoriya et al. 2024; Z. Xu & C.-W. Shu 2024, in preparation).

Here, we follow the pragmatic approach chosen by M. Dumbser et al. (2024), who, motivated by the complexity of the Einstein equations, subtracted the equilibrium solution altogether from the governing PDE; see also L. Pareschi & T. Rey (2017) and J. P. Berberich et al. (2021), therefore solving the following augmented system:

$$\partial_t U + \partial_x F(U) - \partial_x F(U_e) + C(U) \partial_x U - C(U_e) \partial_x U_e = S(U) - S(U_e); \quad \partial_t U_e = 0. \quad (50)$$

In this way, the discretization errors introduced by the numerical scheme are removed and exact equilibrium can be maintained. There is a price to pay, of course, in so far the vector of evolved quantities is effectively doubled, becoming  $\tilde{U} = [U, U_e]$ . The equilibrium sector of the extended vector  $\tilde{U}$ , i.e.,  $U_e$ , is ultimately excluded from the time evolution, but it enters all the spatial discretization procedures of the numerical scheme.

We have added this property to our numerical schemes as an extra feature that can be activated, or not, depending on the problem considered. For more details on the numerical approach, see L. Pareschi & T. Rey (2017), J. P. Berberich et al. (2021), M. Dumbser et al. (2024).

## 4. Numerical Tests

In this section, we explore two distinct computational schemes outlined in Section 3. First, we consider the scheme described by Equation (31), explained in Section 3.2. It is noteworthy that employing a  $k$ th-order accurate WENO-AO reconstruction in Equation (31) results in a  $k$ th-order accurate FD-WENO scheme. We label the resultant scheme as FD-WENO- $k$ . Next, we explore the AFD-WENO scheme outlined in Section 3.4 and defined by Equation (47). The scheme given by Equation (47) usually shows one order of accuracy lower compared to Equation (49); nevertheless, it may have some advantages for GR because, when the solution is smooth, it gives very good quality solutions at a lower computational cost. Implementing a WENO-AO interpolation of order “ $k$ ” in Equation (47) yields a  $(k - 1)$ th order scheme. We label the resultant scheme as AFD-WENO- $(k - 1)$ . For both schemes, we explore the scenarios where  $k$  is set to 3, 5, 7, and 9, providing a comprehensive examination across different order schemes.

In the following, we show the performances of the new schemes over a representative sample of standard tests in NR. While doing so, we are also going to monitor the energy constraint  $H$  and the momentum constraints  $M_i$ , also known as ADM constraints, which, in a vacuum spacetime, are defined as

$$H = R - K_{ij} K^{ij} + K^2, \quad (51)$$

$$M_i = \gamma^{jl} (\partial_l K_{ij} - \partial_i K_{jl} - \Gamma_{jl}^m K_{mi} + \Gamma_{ji}^m K_{ml}). \quad (52)$$



**Table 1**Section 4.1:  $L_1$  Errors,  $L_\infty$  Errors, and the Corresponding Order of Convergence for the Third-, Fifth-, Seventh-, and Ninth-order Accurate FD-WENO Schemes

Scheme	Grid Size	$L_1$ Errors	Order	$L_\infty$ Errors	Order
FD-WENO-3	$32 \times 2$	1.32436e-04	...	2.68393e-04	...
	$64 \times 4$	1.65963e-05	3.00	3.41976e-05	2.97
	$128 \times 8$	2.07707e-06	3.00	4.29149e-06	2.99
	$256 \times 16$	2.59697e-07	3.00	5.36977e-07	3.00
FD-WENO-5	$32 \times 2$	1.41137e-06	...	4.11999e-06	...
	$64 \times 4$	4.42906e-08	4.99	1.31668e-07	4.97
	$128 \times 8$	1.38883e-09	5.00	4.13672e-09	4.99
	$256 \times 16$	4.34472e-11	5.00	1.29485e-10	5.00
FD-WENO-7	$16 \times 1$	9.83235e-06	...	2.75912E-05	...
	$32 \times 2$	4.15493e-08	7.89	1.50863E-07	7.51
	$48 \times 3$	2.43860e-09	6.99	8.53961E-09	7.08
	$64 \times 4$	3.29132e-10	6.96	1.13484E-09	7.02
FD-WENO-9	$8 \times 1$	1.70885e-04	...	3.55896e-04	...
	$16 \times 2$	8.48349e-07	7.65	2.66925e-06	7.06
	$24 \times 3$	2.57895e-08	8.62	9.82247e-08	8.14
	$32 \times 4$	2.17566e-09	8.60	8.25465e-09	8.61

**Note.** The lapse  $\alpha$  variable has been shown. A final time of  $t = 1.0$  has been used for the study.

#### 4.1. Gauge Wave

We start our validation by considering the propagation of a gauge wave, which is generated after a suitable change of coordinates in a flat Minkowski spacetime (M. Alcubierre et al. 2004), producing the following metric:

$$ds^2 = -H(x, t) dt^2 + H(x, t) dx^2 + dy^2 + dz^2,$$

where  $H(x, t) = 1 - A \sin(2\pi(x - t))$ .

(53)

In practice, it describes a sinusoidal wave of amplitude  $A$  that propagates along the  $x$ -axis, with the lapse  $\alpha = \sqrt{H}$  and the extrinsic curvature initialized through its definition  $K_{ij} = -\partial_t \gamma_{ij} / (2\alpha)$ . As reported by several authors, this test cannot be evolved stably and accurately over long timescales by the classical BSSNOK system, either in second- or first-order formulations (M. C. Babiuc et al. 2008; J. D. Brown et al. 2012), while it has been successfully solved within the first-order CCZ4 and Z4 formulations (M. Dumbser et al. 2018, 2024), in both cases with no need to activate the damping mechanisms. We have also solved this problem by selecting  $\kappa_1 = 0$ ,  $\kappa_2 = 0$ , no *gamma driver* ( $s = 0$ ), harmonic gauge conditions, i.e.,  $g(\alpha) = 1$  in Equation (5), and  $c = 1$ . The numerical domain is the rectangle  $[-0.5, 0.5] \times [-0.05, 0.05]$ , which is covered by an  $N_x \times N_y$  uniform grid. Periodic boundary conditions are selected.

This test is also rather useful for validating the order of accuracy of the numerical scheme. We have therefore considered a battery of tests with a short final time,  $t = 1.0$ , producing results that are reported in Tables 1 and 2, corresponding to our FD-WENO and AFD-WENO schemes, respectively. As it can be appreciated, the nominal order of convergence is successfully reproduced.

Figure 4, on the contrary, reports the results obtained with FD-WENO schemes, by showing, in the first column, the numerical errors of the lapse  $\alpha$  with respect to the exact solution at time  $t = 1000$ , for various orders, using a wave

**Table 2**Section 4.1:  $L_1$  Errors,  $L_\infty$  Errors, and the Corresponding Order of Convergence for the Second-, Fourth-, Sixth-, and Eighth-order Accurate AFD-WENO Schemes

Scheme	Grid Size	$L_1$ Errors	Order	$L_\infty$ Errors	Order
AFD-WENO-2	$32 \times 2$	3.45649E-04	...	5.68896E-04	...
	$64 \times 4$	8.25823E-05	2.07	1.34221E-04	2.08
	$128 \times 8$	2.03870E-05	2.02	3.30125E-05	2.02
	$256 \times 16$	5.07952E-06	2.00	8.21743E-06	2.01
AFD-WENO-4	$32 \times 2$	3.69051E-06	...	8.72790E-06	...
	$64 \times 4$	1.98678E-07	4.22	4.35846E-07	4.32
	$128 \times 8$	1.22491E-08	4.02	2.63489E-08	4.05
	$256 \times 16$	7.63165E-10	4.00	1.63497E-09	4.01
AFD-WENO-6	$16 \times 1$	9.80463e-06	...	2.80057e-05	...
	$32 \times 2$	7.37080e-08	7.06	2.24641e-07	6.96
	$48 \times 3$	6.23277e-09	6.09	1.81759e-08	6.20
	$64 \times 4$	1.13379e-09	5.92	3.27951e-09	5.95
AFD-WENO-8	$8 \times 1$	2.77564e-04	...	5.40091e-04	...
	$16 \times 2$	8.74626e-07	8.31	2.78709e-06	7.60
	$24 \times 3$	3.62176e-08	7.85	1.31702e-07	7.53
	$32 \times 4$	4.60690e-09	7.17	1.68872e-08	7.14

**Note.** The lapse  $\alpha$  variable has been shown. A final time of  $t = 1.0$  has been used for the study.

amplitude  $A = 0.1$  and 128 zones. In the right column we display the evolution of the ADM constraints, which remain perfectly under control all along the simulation. Figure 5 serves the same purpose, but this time for the results obtained with AFD-WENO schemes. We note that in such a long simulation both FD-WENO-3 and AFD-WENO-2 schemes lead to relatively large errors at the given resolution, as it is visible from the numbers in the top-left panels of Figures 4 and 5, with a slightly better performance of FD-WENO-3 with respect to AFD-WENO-2. For the higher-order FD-WENO and AFD-WENO schemes ( $k = 5, 7, 9$ ), the numerical solutions reproduce the analytic ones with very good accuracy.

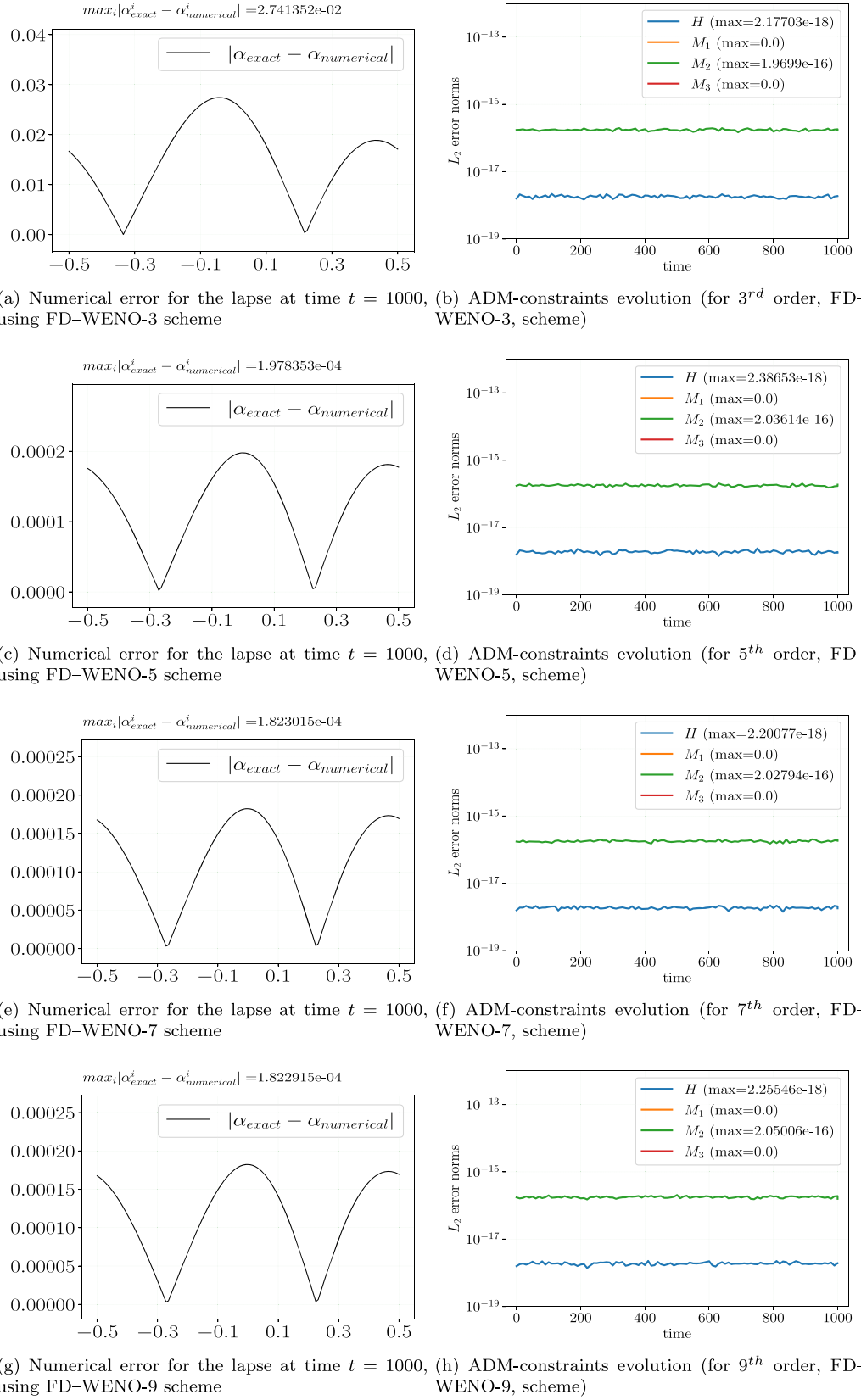
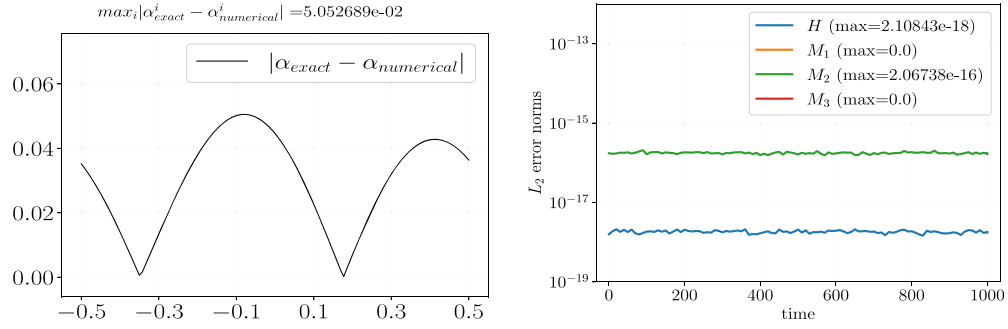


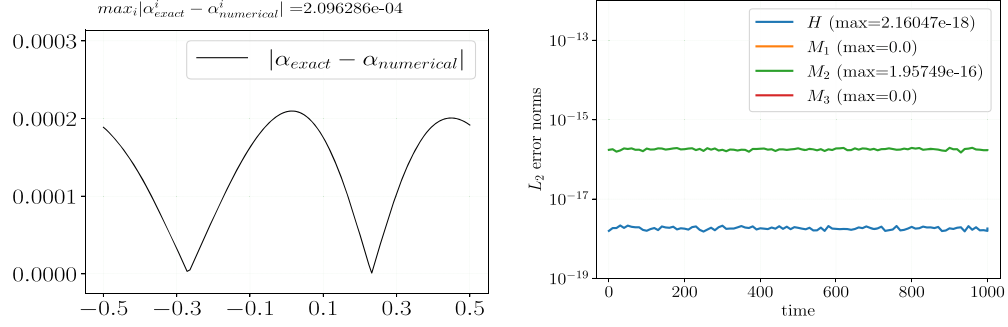
**Figure 4.** Section 4.1: the left panels (a), (c), (e), and (g) show the difference between the numerical solution and the exact one for the variable  $\alpha$  (lapse) at time  $t = 1000$  for various order accurate FD-WENO schemes. The right panels (b), (d), (f), and (h) show the  $L_2$ -error evolution of the ADM constraints for the corresponding order scheme.

In view of possible studies of critical phenomena in gravitational collapse, we have also evolved the same gauge wave but with the  $1+\log$  gauge condition. This gauge

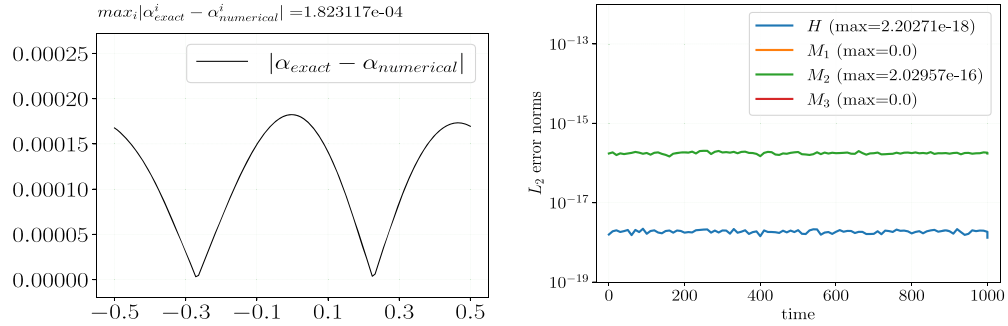
condition is known to produce *gauge shocks* (M. Alcubierre 1997; T. W. Baumgarte & D. Hilditch 2022; T. W. Baumgarte et al. 2023b), which can easily make the code crash. The



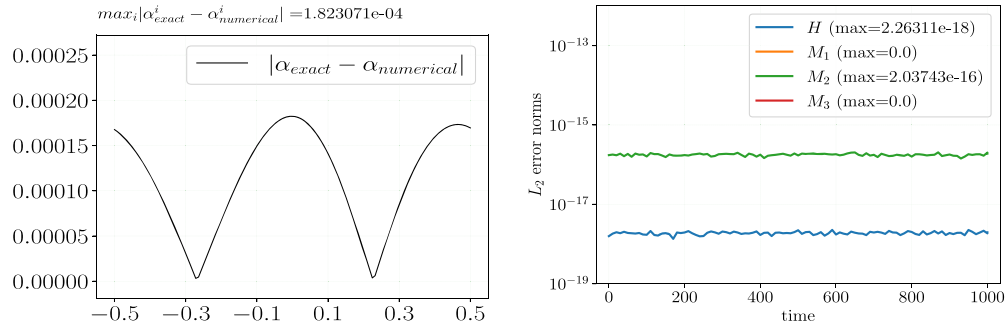
(a) Numerical error for the lapse at time  $t = 1000$ , (b) ADM-constraints evolution (for 2<sup>nd</sup> order, AFD-WENO-2, scheme)



(c) Numerical error for the lapse at time  $t = 1000$ , (d) ADM-constraints evolution (for 4<sup>th</sup> order, AFD-WENO-4, scheme)



(e) Numerical error for the lapse at time  $t = 1000$ , (f) ADM-constraints evolution (for 6<sup>th</sup> order, AFD-WENO-6, scheme)



(g) Numerical error for the lapse at time  $t = 1000$ , (h) ADM-constraints evolution (for 8<sup>th</sup> order, AFD-WENO-8, scheme)

**Figure 5.** Section 4.1: the left panels (a), (c), (e), and (g) show the difference between the numerical solution and the exact one for the variable  $\alpha$  (lapse) at time  $t = 1000$  for various order accurate FD-WENO schemes. The right panels (b), (d), (f), and (h) show the  $L_2$ -error evolution of the ADM constraints for the corresponding order scheme.

results of our computations are shown in Figure 6, where strong gradients are formed in the lapse, but the numerical scheme can still cope with them and the code does not crash, not even after

very long times. Even if at the level of an academic case, this test shows the ability of the Z4 formulation, combined with our numerical scheme, to resolve the propagation of gauge shocks.



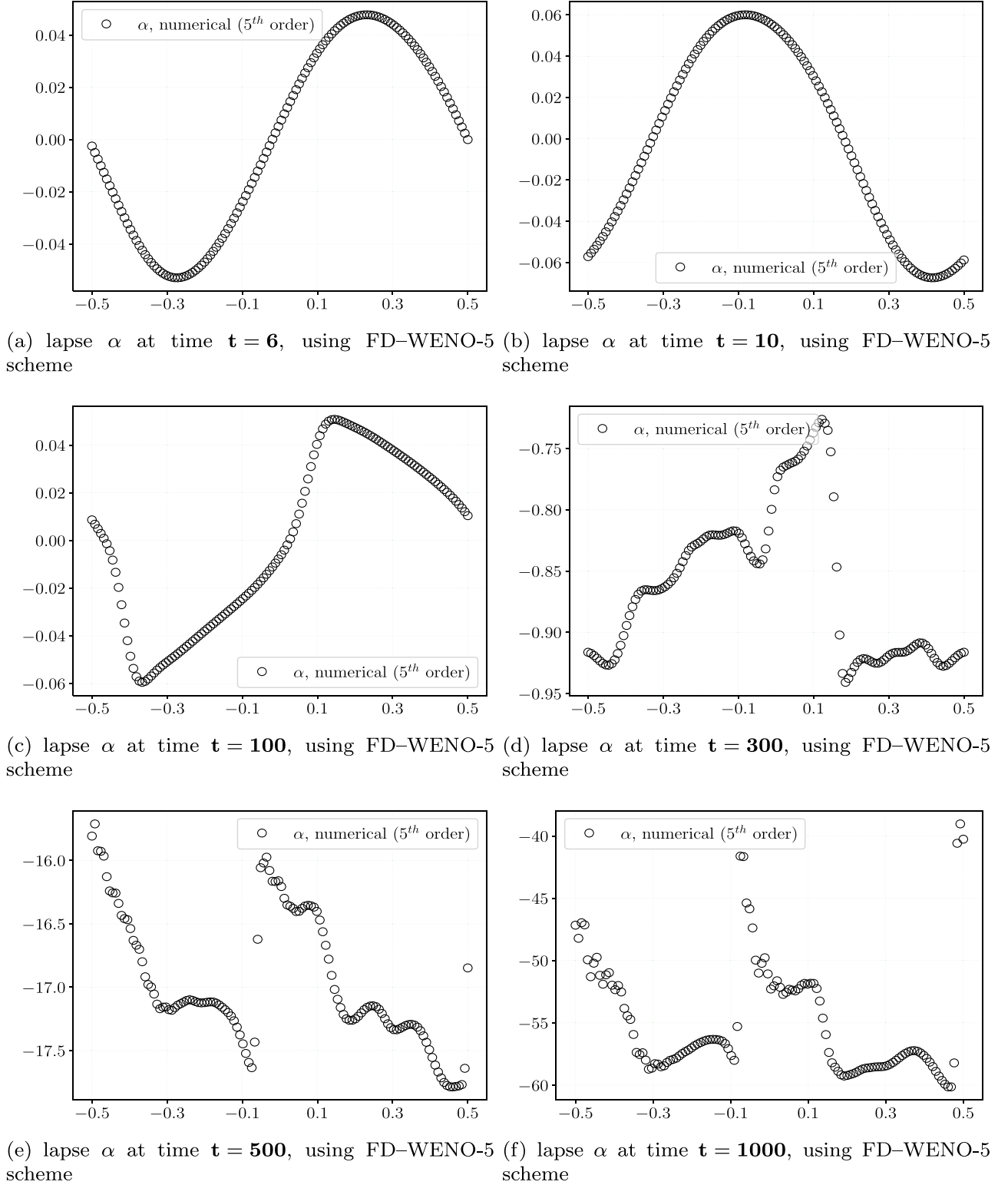


**Figure 6.** Section 4.1: time evolution of the lapse profile  $\alpha$  at different time levels when the  $I+\log$  gauge condition is being used.

Because the shocks are only of modest strength, interpolation on the primal variables was sufficient, and interpolation in characteristic space was not needed.

#### 4.2. Robust Stability Test

The so-called *robust stability test* is used to provide an empiric indication of the hyperbolicity of the PDE system,

and it was introduced when there were very few theoretical analyses of the second-order BSSNOK formulation (H. Beyer & O. Sarbach 2004). In view of the huge progress witnessed by NR in the last 20 yr, and especially because strong hyperbolicity of the present first-order Z4 formulation has been verified by M. Dumbser et al. (2024), this test has lost part of its relevance. Nevertheless, it is still quite useful to

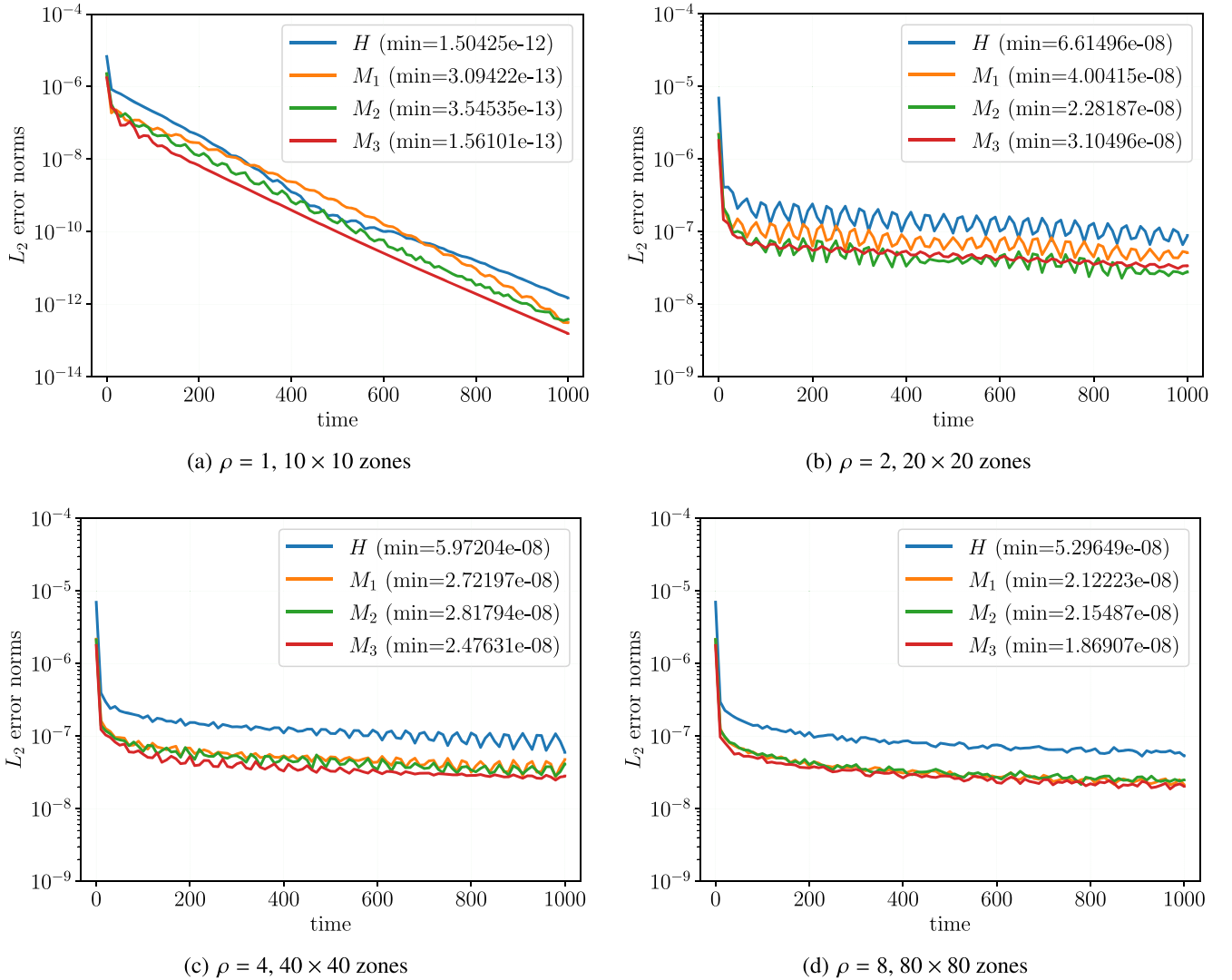


**Figure 7.** Section 4.2: time evolution of  $L_2$  norms of Einstein constraints for the robust stability test with a random initial perturbation of amplitude  $10^{-7}/\rho^2$  in all quantities on a sequence of successively refined meshes on the square domain in 2D. The final time is  $t = 1000$ , and we used a fifth-order accurate FD-WENO scheme (FD-WENO-5) to obtain the results.

exclude possible exponential unstable modes that could be in principle triggered by a given numerical algorithm (G. Calabrese et al. 2006). We should also comment on the fact that, to the best of our knowledge, none of the first-order formulations of the Einstein equations have shown any problem with this test (C. Bona et al. 2004; J. D. Brown et al. 2012; M. Dumbser et al. 2018, 2024). We have therefore prepared the usual setup, given by a flat Minkowski spacetime in two space dimensions, in which all the metric terms are perturbed with a random perturbation of amplitude  $\pm 10^{-7}/\varrho^2$ . The integer  $\rho$  is also used to control the resolution in a set of increasingly refined meshes. The computational domain is given by the square  $[-0.5; 0.5] \times [-0.5; 0.5]$ , with periodic boundary conditions along each direction. As customary for this test, the *gamma driver* is activated, with  $\eta = 0.2$  in Equation (7). The time evolution of the Einstein constraints for the FD-WENO and for the AFD-WENO schemes are shown in Figures 7 and 8, respectively, establishing quite a successful outcome for this test.

### 4.3. Gowdy Wave

There is a relatively simple solution to test the numerical behavior of the PDE system in the strong field regime, and this is given by the so-called Gowdy solution (R. H. Gowdy 1971). It describes a polarized gravitational wave (for us along the  $x$ -direction) via a spacetime metric given by

$$ds^2 = t^{-1/2} e^{Q/2} (-dt^2 + dx^2) + t(e^P dy^2 + e^{-P} dz^2), \quad (54)$$

with

$$P(x, t) = J_0(2\pi t) \cos(2\pi x), \quad (55)$$

$$Q(x, t) = \pi J_0(2\pi) J_1(2\pi) - 2\pi t J_0(2\pi t) J_1(2\pi t) \cos(2\pi x) + 2\pi^2 t^2 [J_0^2(2\pi t) + J_1^2(2\pi t) - J_0^2(2\pi) - J_1^2(2\pi)], \quad (56)$$

where  $J_0$  and  $J_1$  are the Bessel functions (M. Alcubierre et al. 2004; C. Bona et al. 2004). This test becomes interesting when used to simulate the formation of a singularity. This is better

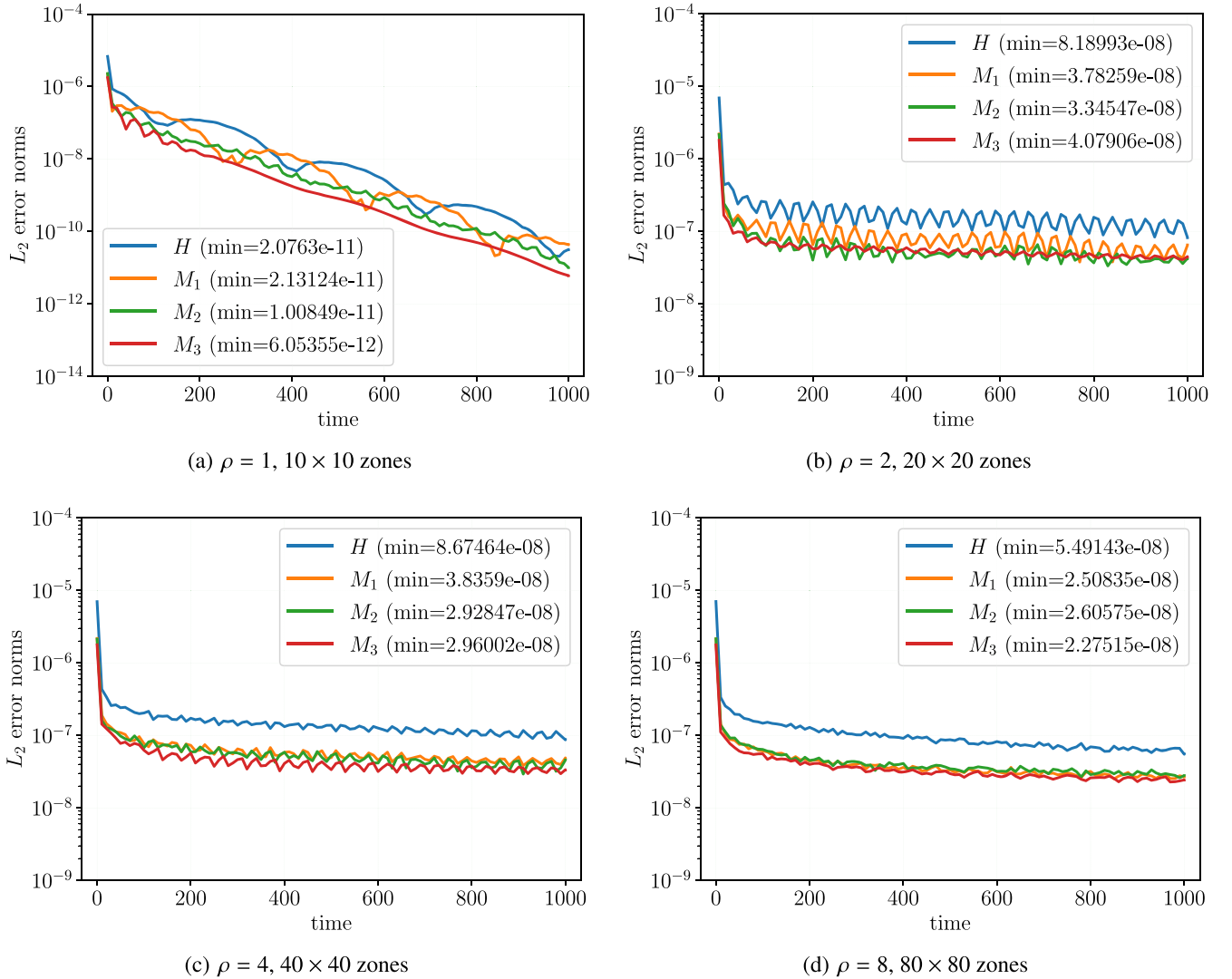


**Figure 8.** Section 4.2: time evolution of  $L_2$  norms of Einstein constraints for the robust stability test with a random initial perturbation of amplitude  $10^{-7}/\rho^2$  in all quantities on a sequence of successively refined meshes on the square domain in 2D. The final time is  $t = 1000$ , and we used a fourth-order accurate AFD-WENO scheme (AFD-WENO-4) to obtain the results.

obtained after performing the time change of coordinate  $t \rightarrow \tau$ , i.e.,

$$t = t_0 e^{-\tau/\tau_0}, \quad (57)$$

implying that the singularity is reached in the limit of  $\tau \rightarrow +\infty$ ,  $\tau$  now being the new time coordinate of the code. Since the roots of  $J_0(2\pi t)$  determine the times at which the lapse is momentarily constant (in space), we conform to the standard choice and we select  $t_0$  as the 20th root of  $J_0(2\pi t)$ , giving  $t_0 = 9.8753205829098$ . The corresponding value of the lapse resulting from the coordinate transformation (Equation (57)) is  $\alpha = t^{3/4} e^{Q/4}/\tau_0$ , and, after imposing  $\alpha = 1$  at  $\tau = 0$  ( $t = t_0$ ), we get the value  $\tau_0 = 471.806749033034$ . The time coordinate transformation does not affect the metric terms  $\gamma_{ij}$ , which follow directly from Equation (54), while the extrinsic curvature can be easily computed from the definition  $K_{ij} = -1/(2\alpha)\partial_\tau \gamma_{ij}$ . The simulation then starts at  $\tau = 0$ , reaching the singularity in the limit of  $\tau \rightarrow +\infty$  ( $t \rightarrow 0$ ).

We have solved this test as a one-dimensional problem using a mesh composed of 120 zones, up to the final time  $\tau = 1000$ . We impose periodic boundary conditions. In Figures 9 and 10, we show the results obtained with our FD-WENO and AFD-WENO schemes, respectively. The left panels report the numerical error of the variable  $K_{xx}$  at the final time. The right panels, on the other hand, show the evolution of the Einstein constraints, which, in spite of a linear increase already documented in the literature (C. Bona et al. 2004), remain under control.

#### 4.4. Stationary Black Holes

Contrary to naive expectations, keeping a simple Schwarzschild or Kerr black hole stationary in three dimensions via an NR code is far from trivial. In this subsection, we refer to the stationary BH solutions of Schwarzschild (1916) and R. P. Kerr (1963), both of them in horizon penetrating coordinates, and not to puncture black holes. Within the second-order BSSNOK formulation, promising attempts were performed by M. Alcubierre & B. Brügmann (2001), who, however, performed the

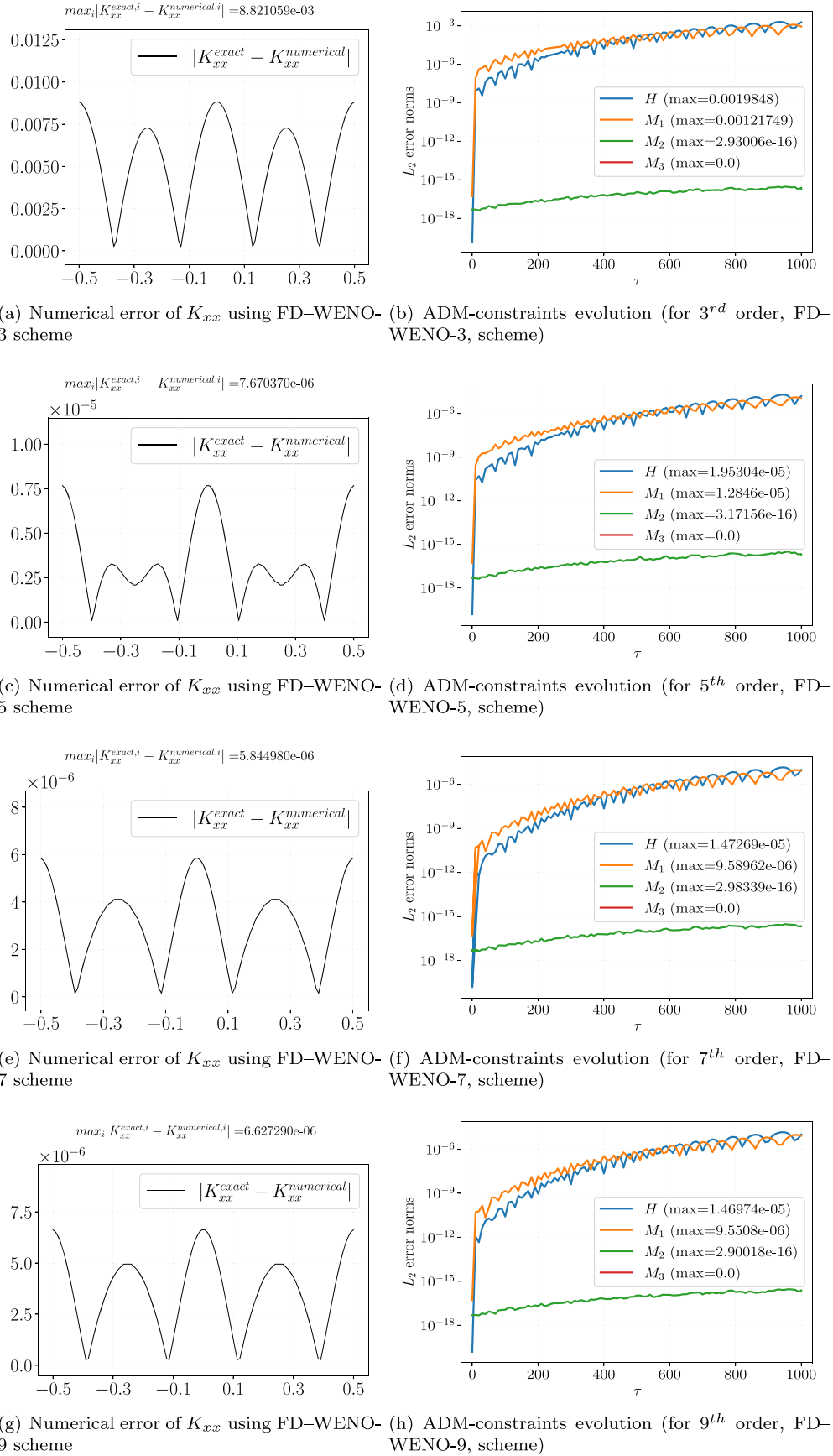


**Figure 9.** Section 4.3: the left panels (a), (c), (e), and (g) show the difference between the numerical solution and the exact one for the variable  $K_{xx}$  at time  $\tau = 1000$  for various order accurate FD-WENO schemes. The right panels (b), (d), (f), and (h) show the  $L_2$ -error evolution of the ADM constraints at the corresponding order.



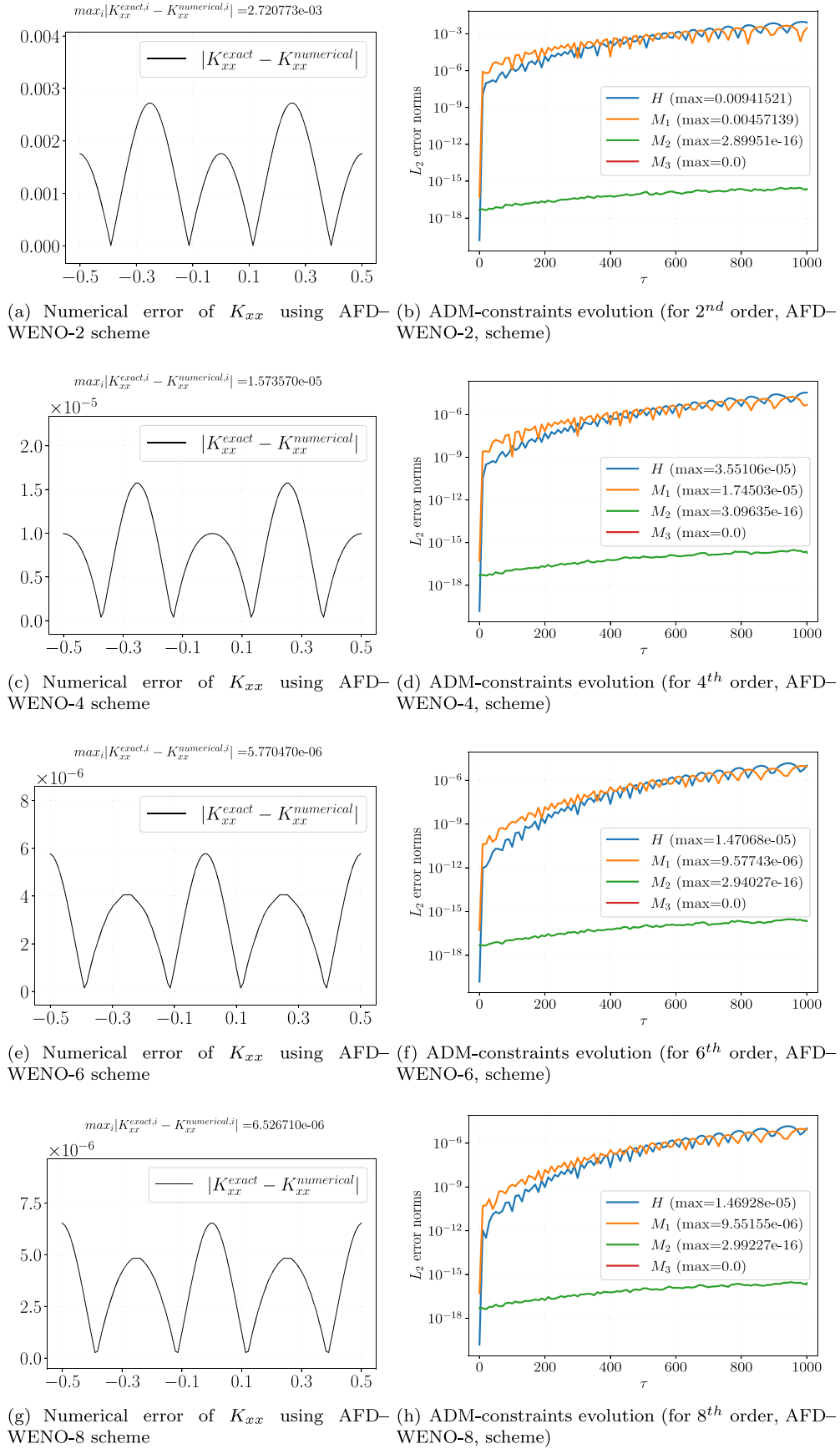


**Figure 10.** Section 4.3: the left panels (a), (c), (e), and (g) show the difference between the numerical solution and the exact one for the variable  $K_{xx}$  at time  $\tau = 1000$  for various order accurate AFD-WENO schemes. The right panels (b), (d), (f), and (h) show the  $L_2$ -error evolution of the ADM constraints at the corresponding order.

calculations on one octant only (because of spherical symmetry) while they reported the appearance of an unstable mode when they extended the simulation in the full grid space. Substantial progress is reported in W. Tichy (2009), with the Hamiltonian constraint that, however, manifests an exponential growth on long timescales. In 2001, after using an alternative first-order formulation of the Einstein equations, henceforth the Kidder–Scheel–Teukolsky formulation, L. E. Kidder et al. (2001) were able to evolve a Schwarzschild black hole in three space dimensions, though the momentum constraints did not seem to be fully under control. Better results were obtained by B. Brügmann (2013), who kept a Schwarzschild black hole in spherical Kerr–Schild coordinates stationary for very long timescales, using spectral methods in combination with a first-order formulation of the Einstein equations in the generalized harmonic gauge. Again in this formulation, W. Tichy et al. (2023) obtained rather good results as well for a nonrotating black hole, but using DG methods. Finally, after using a well-balanced version of the first-order Z4 formulation of the Einstein equations, in combination with an ADER-DG scheme, M. Dumbser et al. (2024) were able to preserve perfect stationary equilibria of even extreme Kerr black holes over arbitrarily long timescales.

We have therefore considered the stationary solution represented by the Kerr spacetime in pseudo-Cartesian Kerr–Schild coordinates, as they can be found, for instance, in F. de Felice & C. J. S. Clarke (1990) (Section 11.4) or in D. L. Wilshire et al. (2009). Here, we reconsider that problem by adopting a seventh-order FD-WENO scheme and a sixth-order AFD-WENO scheme, applied in three-dimensional (spatial) simulations. The three-dimensional computational domain is given by  $\Omega = [-5; 5]^3$  covered by an  $80 \times 80 \times 80$  uniform grid, while, as boundary conditions, we impose the stationary equilibrium solution at the outer border. The gauge condition adopted is the *1+log gauge condition*. We also recall that, in the coordinates adopted, the physical singularity is mapped into the so-called ring singularity in the  $z=0$  plane, with a radius given by the spin of the black hole. For this reason, we have excised the ring singularity from the numerical domain, which remains inside an appropriate excision box. Moreover, we insert an initial perturbation in the cleaning variable  $\Theta$ , which is chosen as

$$\Theta(t=0) = A_0 \exp \left( -\frac{1}{2} \frac{(x-2.5)^2 + (y-0)^2 + (z-0)^2}{\sigma^2} \right), \quad (58)$$

with  $A_0 = 10^{-3}$ ,  $\sigma = 0.2$ . We have found it crucial for a successful evolution of these equilibrium tests over arbitrarily long times to activate the *well-balancing* property described in Section 3.5. Without well-balancing, small but ever-growing deviations from equilibrium were detected on times  $t \geq 100$ , even at the sixth order of convergence of our numerical schemes. Under these settings, we have considered the following two representative cases:

1. A *Schwarzschild black hole* ( $a=0$ ). Figures 11 and 12 show the results of a long run with  $t_f = 1000 M$ , obtained with the FD-WENO scheme and with the AFD-WENO scheme, respectively. The central top panel reports a contour-color representation of the lapse  $\alpha$  through the

$z=0$  plane, while the arrows visualize the vector field of the shift  $\beta^i$ , which, in spite of the black hole being non/rotating, is nonzero due to the choice of the coordinates. The remaining panels, with 1D profiles along the  $z$ -axis, show the numerical error of three representative quantities at the final time  $t = 1000$  with respect to the initial equilibrium solution.

2. A *Kerr black hole* ( $a=0.9$ ). In a rather similar way, Figures 13 and 14 show the results of a long run with  $t_f = 1000 M$ , obtained with the FD-WENO scheme and with the AFD-WENO scheme, respectively. The vector field of the shift, represented in the central top panels of those figures, manifests the clockwise rotation of the black hole.

Finally, the bottom-right panels of Figures 11–14 monitor the evolution of the constraint violations  $H(t) - H(0)$  and  $M_i(t) - M_i(0)$  for the Hamiltonian and the momentum constraints. As can be seen, the effects of the introduced perturbation decay exponentially and the solution converges back to the exact equilibrium. These results confirm what was also found by M. Dumbser et al. (2024).

#### 4.5. Head-on Collision of Two Black Holes

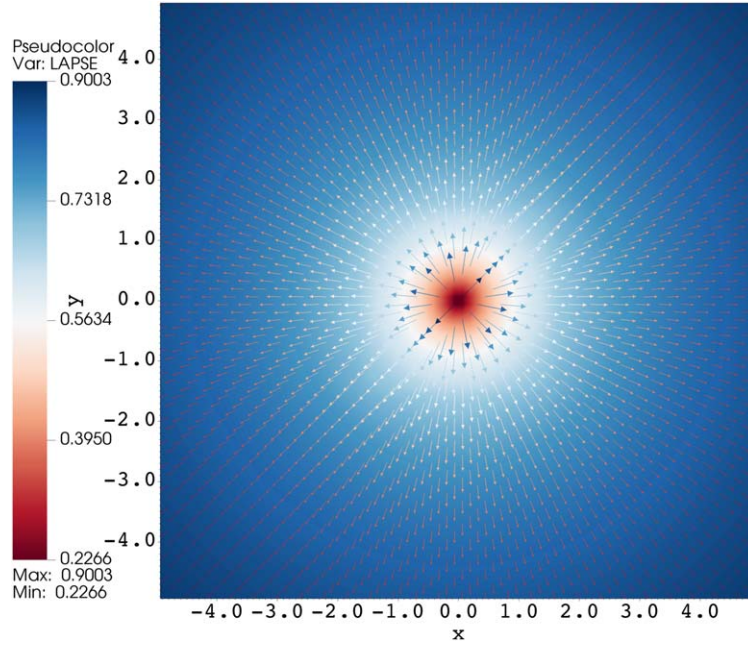
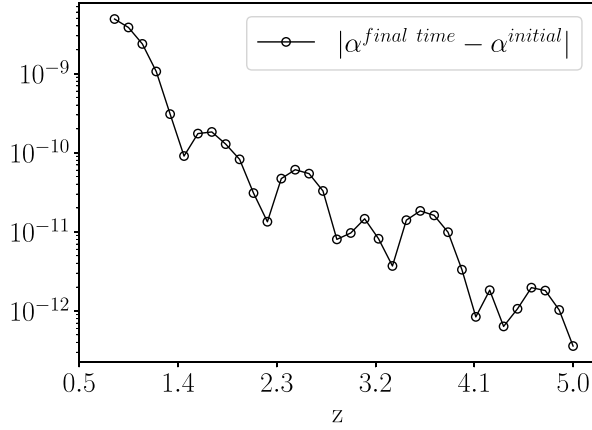
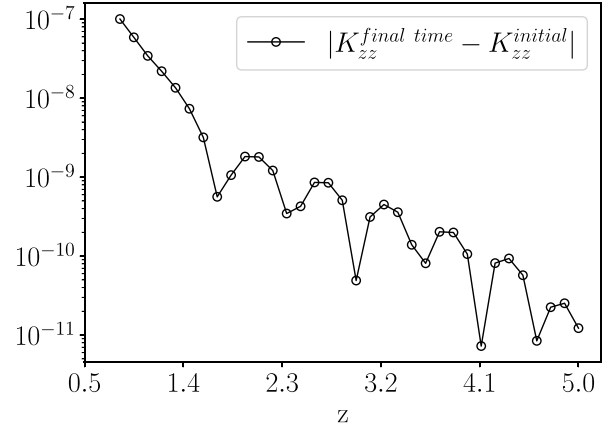
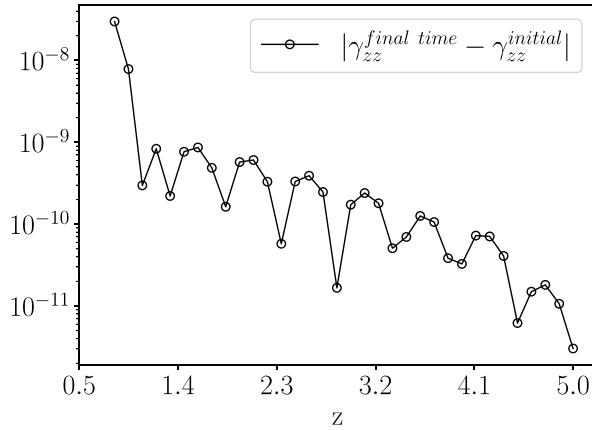
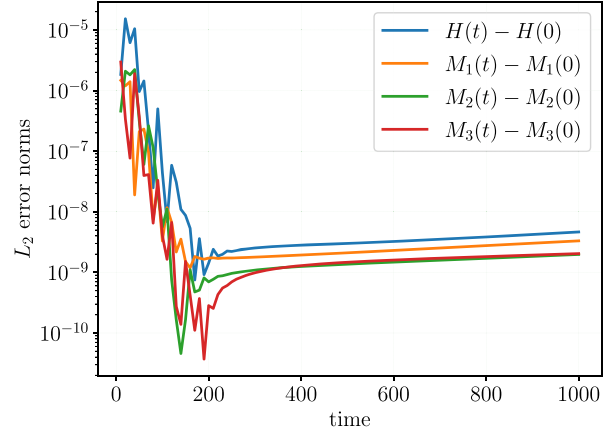
The correct simulation of binary mergers (either black holes or neutron stars) is of course the final goal of NR, which is proving to be an invaluable scientific tool in the preset gravitational-wave era (B. P. Abbott et al. 2019). In this work, still at the level of an exploratory calculation, before a dedicated analysis is performed, we have considered the head-on collision of two nonrotating black holes, which are modeled as two moving punctures. We compute the initial conditions through the `TwoPunctures` initial data code of M. Ansorg et al. (2004), selecting two black holes with equal masses,  $M_1 = M_2 = 1$ , initial positions given by  $\mathbf{x}^- = (-1, 0, 0)$  and  $\mathbf{x}^+ = (+1, 0, 0)$ , zero individual spins and zero linear momenta.<sup>5</sup>

The three-dimensional computational domain is given by  $\Omega = [-15; 15]^3$  covered by an  $80 \times 80 \times 80$  uniform grid, while outgoing boundary conditions are imposed at the border of the computational domain. As shown by M. Dumbser et al. (2024), to avoid division by zero at time  $t=0$  we find it useful to filter the lapse as

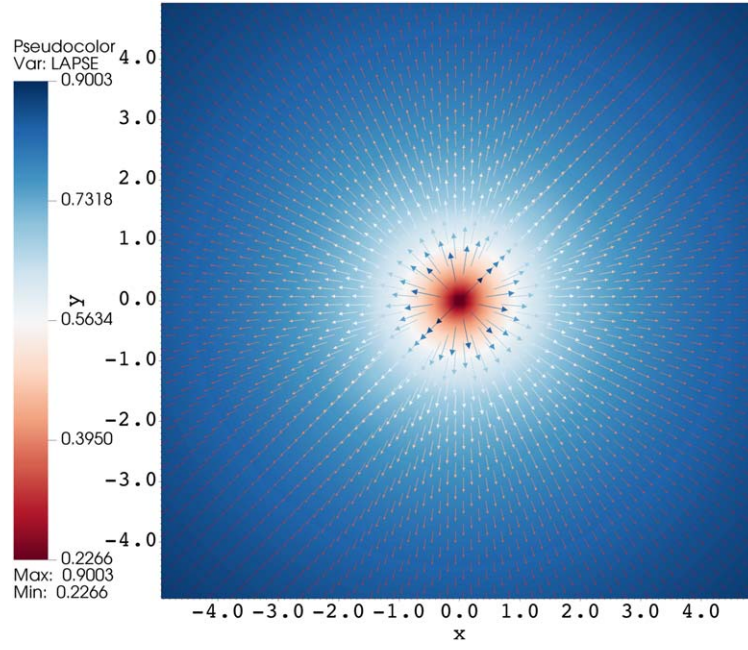
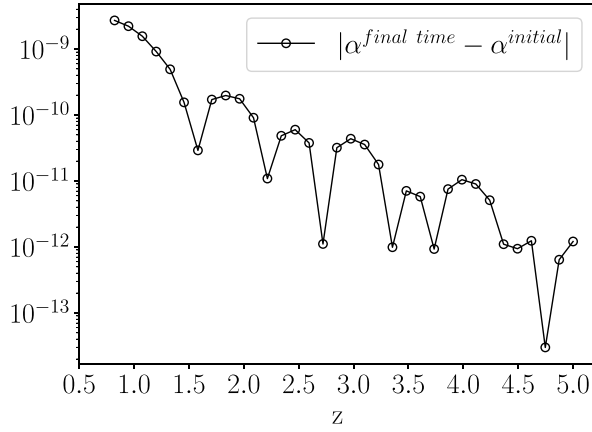
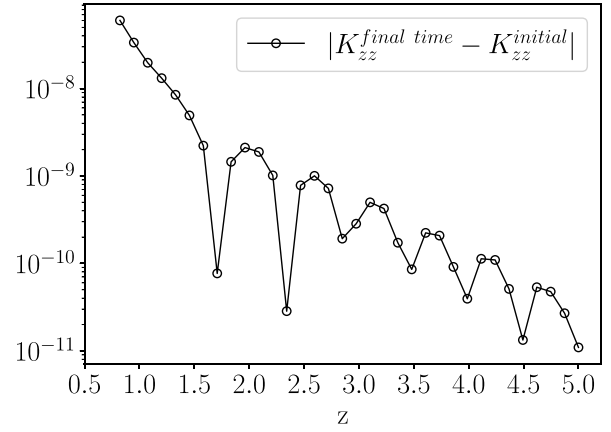
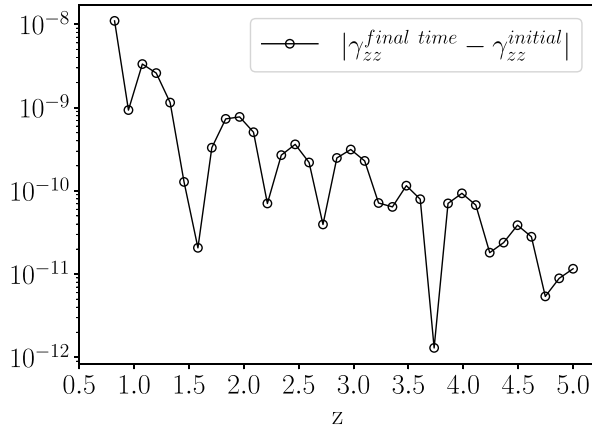
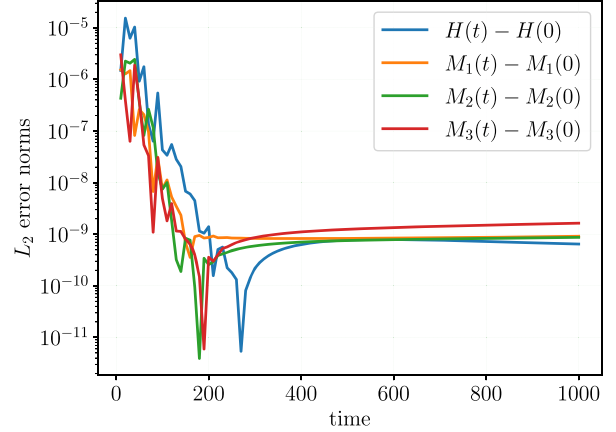
$$\alpha = \frac{\alpha r^6 + \epsilon \alpha_{\min}}{r^6 + \epsilon}, \quad (59)$$

where  $\alpha_{\min} = 0.01$ ,  $\epsilon = 10^{-4}$ . Moreover, during the time evolution, all the metric terms are naturally smoothed out by the *numerical dissipation* present in our Riemann-solver-based FD-WENO schemes. Note that the use of approximate Riemann solvers means upwinding, which is dissipative, and that WENO is a nonlinear shock-capturing feature for high-order schemes that has been deliberately designed to deal with discontinuities and singularities within the discrete solution. This avoids metric spikes, reaching a rather smooth maximum value at  $\gamma_{\max} \sim 25$ . With these caveats, we have solved this test using  $\kappa_1 = 0.2$ ,  $\kappa_2 = 0.2$ ,  $c = 0$ ,  $\mu = 0.1$ , and with the *gamma driver* activated. The results of our calculations are reported in

<sup>5</sup> As an alternative way to obtain the initial conditions, one could also adopt the analytic prescription introduced by D. R. Brill & R. W. Lindquist (1963). See also M. Alcubierre et al. (2003).

(a)  $\alpha$ , lapse profile at  $t = 1000$  (slice plot) and vector field of the shift.(b) profile of the lapse error along  $x = y = 0$ .(c) profile of the  $K_{zz}$  error along  $x = y = 0$ .(d) profile of the  $\gamma_{zz}$  error along  $x = y = 0$ .(e) Evolution of  $L_2$ -error norms for the ADM-constraints

**Figure 11.** Schwarzschild black hole: panels (a)–(d) show the absolute errors of  $\alpha$ ,  $K_{zz}$ , and  $\gamma_{zz}$  for the Schwarzschild black hole ( $a = 0$ ), computed with respect to the exact solution at the final time  $t = 1000$ . Panel (e) shows the violation of the ADM constraints. A seventh-order accurate FD-WENO scheme has been used.

(a)  $\alpha$ , lapse profile at  $t = 1000$  (slice plot) and vector field of the shift.(b) profile of the lapse error along  $x = y = 0$ .(c) profile of the  $K_{zz}$  error along  $x = y = 0$ .(d) profile of the  $\gamma_{zz}$  error along  $x = y = 0$ .(e) Evolution of  $L_2$ -error norms for the ADM-constraints

**Figure 12.** Schwarzschild black hole: panels (a)–(d) show the absolute errors of  $\alpha$ ,  $K_{zz}$ , and  $\gamma_{zz}$  for the Schwarzschild black hole ( $a = 0$ ), computed with respect to the exact solution at the final time  $t = 1000$ . Panel (e) shows the violation of the ADM constraints. A sixth-order accurate AFD-WENO scheme has been used.



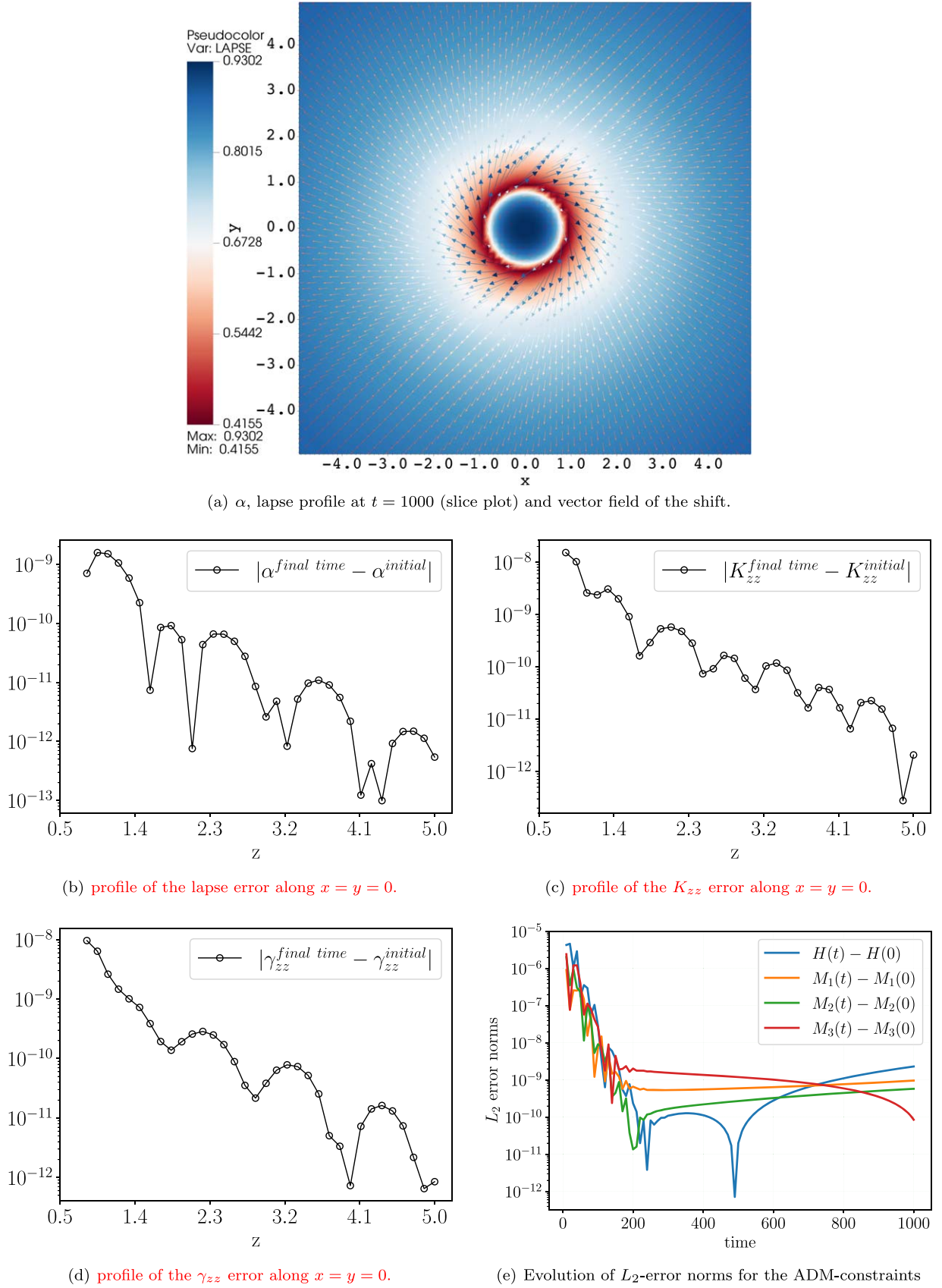


**Figure 13.** Kerr black hole: panels (a)–(d) show the absolute errors of  $\alpha$ ,  $K_{zz}$ , and  $\gamma_{zz}$  for the Kerr black hole ( $a = 0.9$ ), computed with respect to the exact solution at the final time  $t = 1000$ . Panel (e) shows the violation of the ADM constraints. A seventh-order accurate FD-WENO scheme has been used.

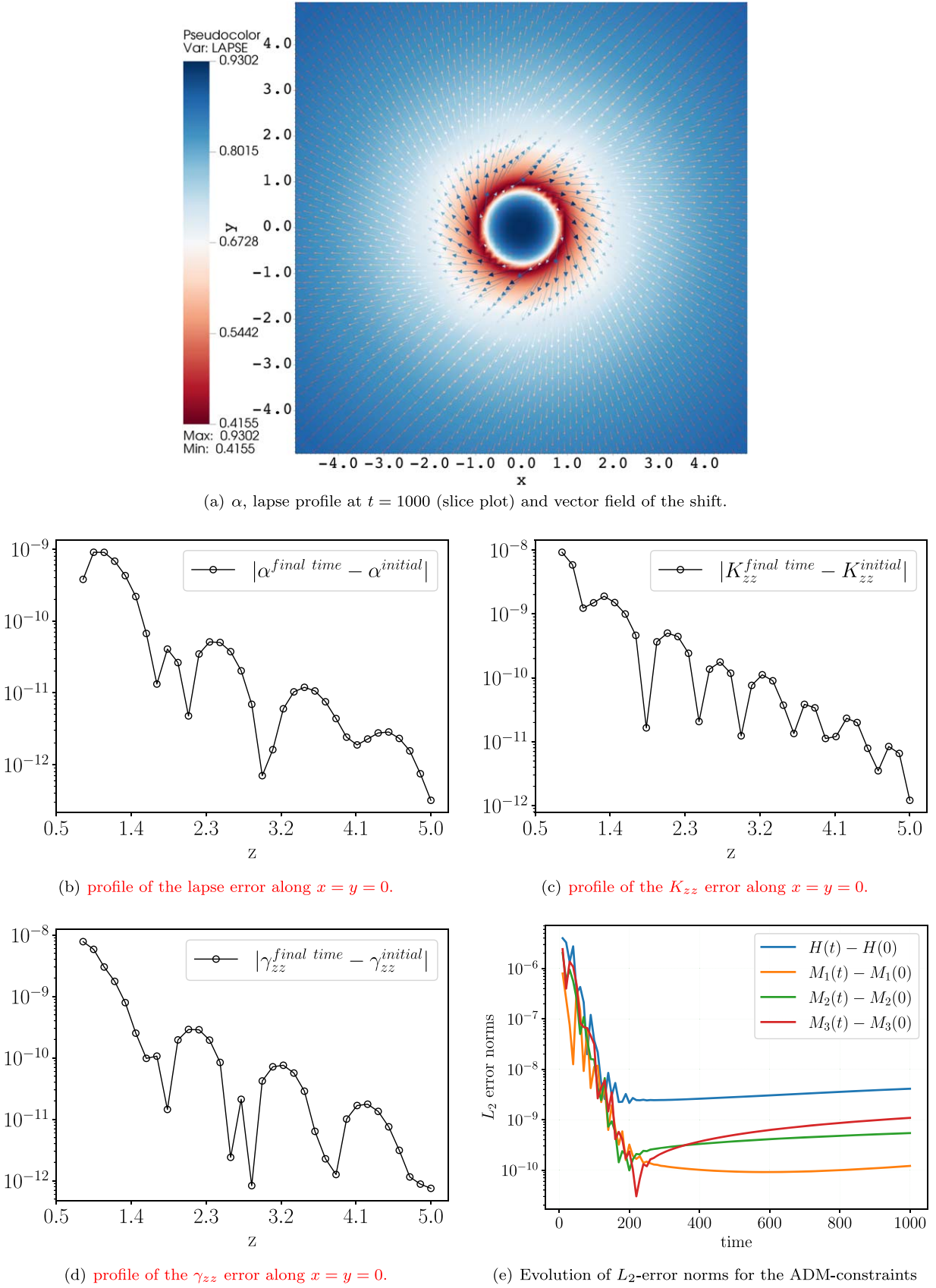


**Figure 14.** Kerr black hole: panels (a)–(d) show the absolute errors of  $\alpha$ ,  $K_{zz}$ , and  $\gamma_{zz}$  for the Kerr black hole ( $a = 0.9$ ), computed with respect to the exact solution at the final time  $t = 1000$ . Panel (e) shows the violation of the ADM constraints. A sixth-order accurate AFD-WENO scheme has been used.

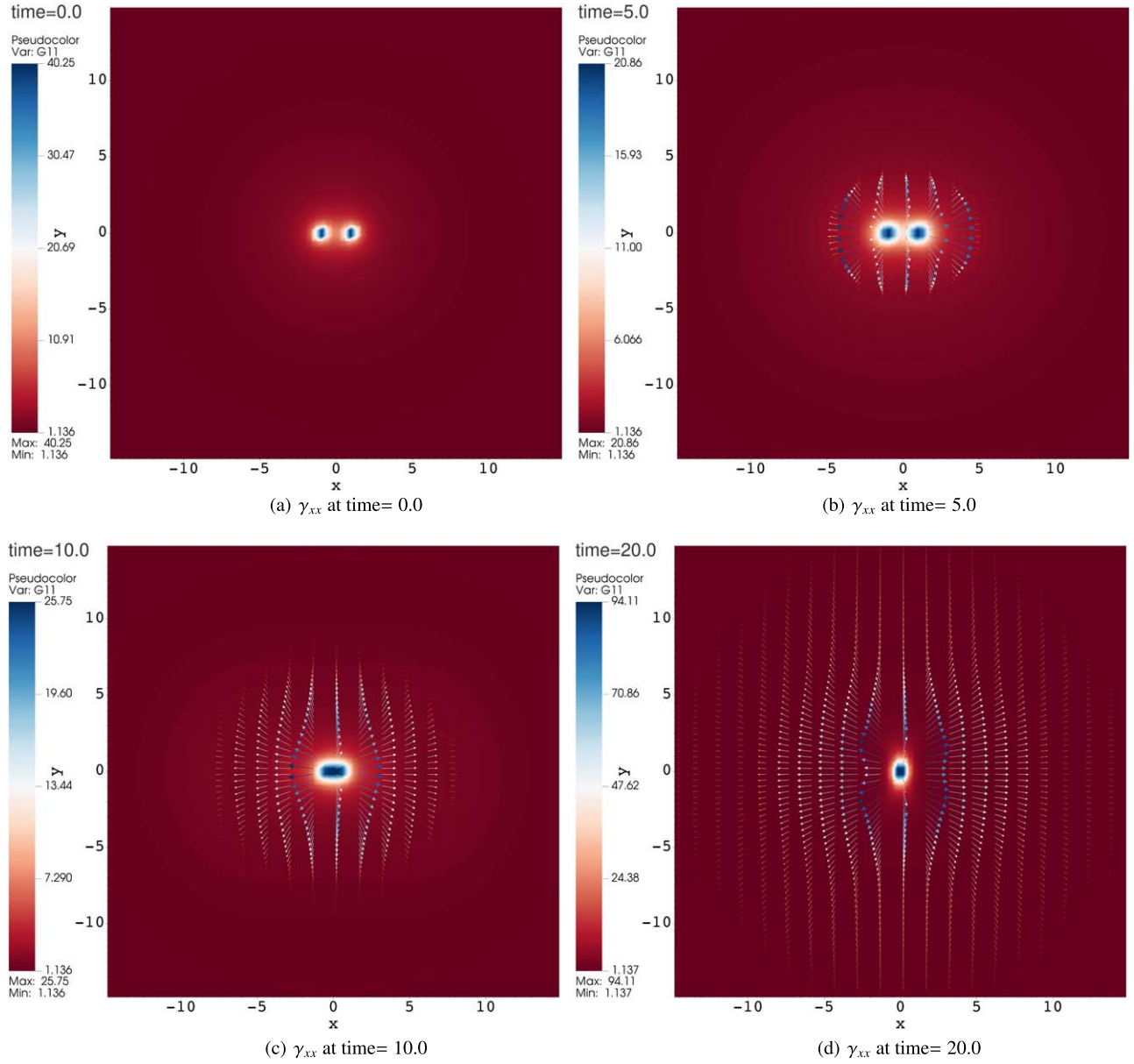


**Figure 15.** Section 4.5: profiles for the metric term  $\gamma_{xx}$  shown at various time levels ( $t = 0, 5, 10, 20$ ). The computations were performed using a ninth-order accurate FD-WENO scheme.

Figures 15 and 16, respectively, where the contour plots of  $\gamma_{xx}$ , as well as the shift vector field, are shown at four representative times. Figure 15 refers to the calculations performed with the FD-WENO scheme, while Figure 16 refers to those obtained with the AFD-WENO scheme.

By the time  $t \sim 10$  (with units of time being  $M_1 = M_2$ ), the merger of the two black holes is almost complete, and a single black hole is hence produced, remaining stationary for longer times. The vector field of the shift  $\beta^i$  manifests the expected behavior, being oriented in the opposite direction with respect to the merger.

## 5. Conclusions

Advances in the sensitivities of gravitational-wave interferometers are such that they will make it possible to make very accurate observations. As a result, we will soon need very high-order schemes for NR that can match those accurate

observations. This motivated us to look at suitable high-order accurate discretizations of first-order formulations of the Einstein field equations. Because first-order formulations have a hyperbolic PDE structure that is common to other very well-explored PDE systems, higher-order solution methods have been very well-developed for this class of problems. Therefore, it is very attractive to look at high-accuracy methods for solving first-order hyperbolic PDE systems. The well-developed higher-order methodologies include DG schemes, finite-volume WENO schemes, and FD-WENO schemes. All three of these classes of schemes present natural pathways to a high order of accuracy in space. However, the first-order formulations for numerical GR have the additional complication that they result in extremely large nonconservative hyperbolic PDE systems. These systems are indeed so large that the memory requirements for DG, and perhaps even finite-volume WENO schemes, are quite demanding. This forces us to take a hard look at recent advances in FD-WENO schemes.

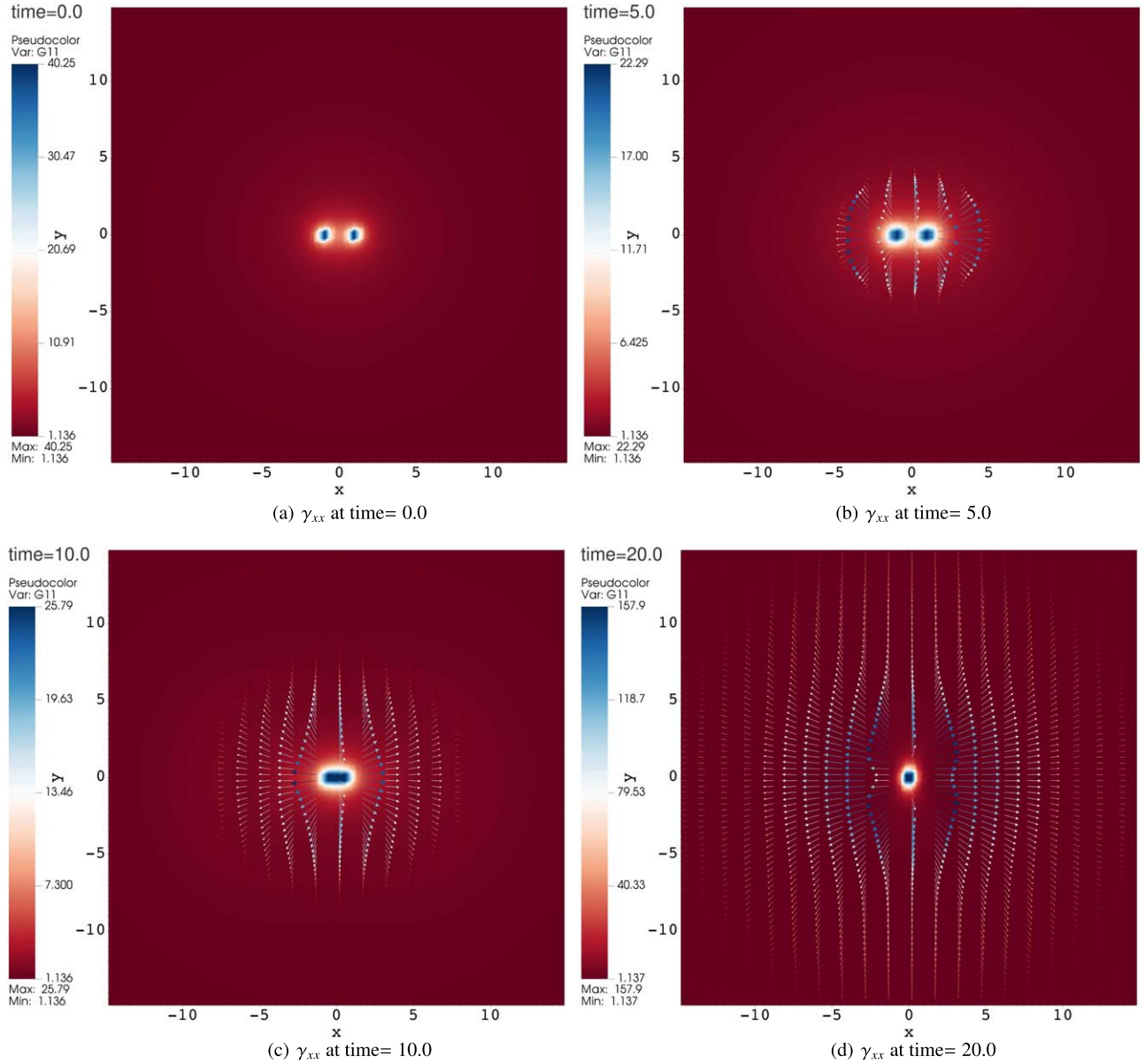


**Figure 16.** Section 4.5: profiles for the metric term  $\gamma_{xx}$  shown at various time levels ( $t = 0, 5, 10, 20$ ). The computations were performed using an eighth-order accurate AFD-WENO scheme.

The Z4 formulation of the Einstein equations, written as a first-order system, naturally gives rise to a hyperbolic PDE system, which we have indicated with the acronym FO-Z4 and that is briefly described in Section 2. While the original Z4 system was proposed in first-order *conservative* form by C. Bona et al. (2004) and C. Bona & C. Palenzuela-Luque (2005), a close analysis performed by M. Dumbser et al. (2024) has shown that its hyperbolicity is better preserved when it is cast as a hyperbolic PDE system in *nonconservation* form. This is of course problematic from the numerical viewpoint because FD-WENO methods for systems that are in nonconservation form are not well known to the astrophysical community and general-purpose solution methods for PDEs with nonconservative products have only been recently discovered. It is, therefore, of great value to the astrophysical community that these methods should all be concatenated in one place and shown to work for the FO-Z4 system of GR. While we focus on the FO-Z4 system, the methods that we present here are much

more broadly useful for any first-order formulation of GR. Indeed, the Introduction documents other first-order formulations for GR that also result in hyperbolic PDEs with nonconservative products.

Section 3 shows us the different FD-WENO technologies that are at our disposal. These bifurcate broadly into FD-WENO schemes that are based on higher-order reconstruction and AFD-WENO schemes that are based on higher-order interpolation. FD-WENO schemes are described in Sections 3.1 and 3.2. The FD-WENO scheme in Section 3.2 is particularly easy to implement, very low cost, and especially useful when the relativistic hydrodynamical equations do not need to be solved in conjunction with the Einstein field equations. But we also realize that the relativistic hydrodynamic equations are naturally written in conservation law form. As a result, we will quite frequently need the AFD-WENO formulation that is described in Sections 3.3 and 3.4. While AFD-WENO schemes cost marginally more than their FD-



WENO cousins, they have the great advantage that they can retrieve a conservation form when conservation needs to be respected in the physical problem. We also present discussions on reconstruction, interpolation, nonlinear hybridization, and upwinding, which are all the algorithmic niceties that a robust high-order scheme must have if it is to operate stably. Visual descriptions of the algorithms have also been provided in Figures 1, 2 and 3 in order to make the methods accessible to the greater community.

It is also worth pointing out that these days, one desires not just a baseline scheme but also an ecosystem of supporting ideas around the baseline scheme. Examples of this ecosystem of ideas include well-balancing, physical constraint preservation, and divergence- and curl-free evolution of vector fields. Wherever possible, we have documented the additional availability of this ecosystem of supporting capabilities for the FD-WENO and AFD-WENO schemes described here.

We have therefore implemented the FD-WENO and AFD-WENO schemes in a three-dimensional code that uses Cartesian coordinates within the standard 3+1 foliation of spacetime. We have successfully reproduced some of the most relevant standard tests of NR in vacuum, as outlined in M. Alcubierre et al. (2004), which include a gauge wave, the robust stability test, the Gowdy wave, stationary isolated black holes (with excision), and a simple head-on collision of two puncture black holes (M. Ansorg et al. 2004). Concerning the gauge wave, we could evolve it on a long timescale with very small deviations from the analytic solution, provided the order of the scheme is at least 4. This points once more to the conclusion that a high order of accuracy might become absolutely crucial in NR. Concerning single stationary black holes (not of puncture type but rather the exact solution of R. P. Kerr 1963), we could evolve them stably over long timescales, thus confirming the positive results obtained by M. Dumbser et al. (2024), who also adopted the same FO-Z4 formulation, but with an entirely different numerical scheme. In this test case, just like in M. Dumbser et al. (2024), we had to augment our numerical scheme with a suitable *well-balancing* feature, in such a way as to preserve perfect stationarity. We recall that, on the contrary, the standard BSSNOK formulation has known problems in performing such a test. Academic as it may seem at first sight, this test is nevertheless very important since it opens the door to a rather accurate numerical study of the normal modes of oscillations of black holes (E. Berti et al. 2009; L. A. H. Mamani et al. 2022). Finally, concerning binary black hole mergers, we confirm the ability of the FO-Z4 formulation in treating simple setups with two moving punctures. However, the lack of the conformal factor, which is typical of this formulation, must be compensated by appropriate filtering of the metric spikes that might be produced during the merger. Further investigations are required to make this approach more efficient while at the same time physically neutral.





### Acknowledgments

This work was financially supported by the Italian Ministry of Education, University and Research (MIUR) in the framework of the PRIN 2022 project High order structure-preserving semi-implicit schemes for hyperbolic equations, by the European Union—Next Generation EU, Mission 4 Component 2-CUP E53D23005840006, and via the Departments of Excellence Initiative 2018–2027 attributed to DICAM of the

University of Trento (grant L. 232/2016). M.D. was also funded by the European Union NextGenerationEU project PNRR Spoke 7 CN HPC and by the European Research Council (ERC) under the European Union’s Horizon 2020 research and innovation programme, grant agreement No. ERC-ADG-2021-101052956-BEYOND. D.S.B. acknowledges support via NSF grant NSF-AST-2009776, NASA grant NASA-2020-1241, and NASA grant 80NSSC22K0628.

We acknowledge the CINECA award under the ISCRA initiative for the availability of high-performance computing resources and support.

### ORCID iDs

Dinshaw Balsara  <https://orcid.org/0000-0003-3309-1052>  
 Deepak Bhoriya  <https://orcid.org/0000-0003-2849-9045>  
 Olindo Zanotti  <https://orcid.org/0000-0003-4307-6809>  
 Michael Dumbser  <https://orcid.org/0000-0002-8201-8372>

### References

- Abbott, B. P., Abbott, R., Abbott, T. D., et al. 2019, *PhRvX*, **9**, 031040
- Alcubierre, M. 1997, *PhRvD*, **55**, 5981
- Alcubierre, M. 2003, *CQGra*, **20**, 607
- Alcubierre, M., Allen, G., Bona, et al. 2004, *CQGra*, **21**, 589
- Alcubierre, M., & Brügmann, B. 2001, *PhRvD*, **63**, 104006
- Alcubierre, M., Brügmann, B., Diener, P., et al. 2003, *PhRvD*, **67**, 084023
- Alcubierre, M. 2008, *Introduction to 3+1 Numerical Relativity* (Oxford: Oxford Univ. Press)
- Alic, D., Bona, C., & Bona-Casas, C. 2009, *PhRvD*, **79**, 044026
- Alic, D., Bona-Casas, C., Bona, C., Rezzolla, L., & Palenzuela, C. 2012, *PhRvD*, **85**, 064040
- Alic, D., Kastaun, W., & Rezzolla, L. 2013, *PhRvD*, **88**, 064049
- Ansorg, M., Brügmann, B., & Tichy, W. 2004, *PhRvD*, **70**, 064011
- Audusse, E., Bouchut, F., Bristeau, M.-O., Klein, R., & Perthame, B. 2004, *SJSC*, **25**, 2050
- Babiuc, M. C., Husa, S., Alic, D., et al. 2008, *CQGra*, **25**, 125012
- Balsara, D. S. 2010, *JCoPh*, **229**, 1970
- Balsara, D. S. 2012, *JCoPh*, **231**, 7504
- Balsara, D. S. 2014, *JCoPh*, **277**, 163
- Balsara, D. S., Bhoriya, D., Shu, C.-W., & Kumar, H. 2023a, *CAMCS*, **6**, 907
- Balsara, D. S., Bhoriya, D., Shu, C.-W., & Kumar, H. 2024a, *CAMCS*, in press
- Balsara, D. S., Bhoriya, D., Shu, C.-W., & Kumar, H. 2024b, *CAMCS*, in press
- Balsara, D. S., Garain, S., & Shu, C.-W. 2016, *JCoPh*, **326**, 780
- Balsara, D. S., & Käppeli, R. 2022, *ApMaC*, **4**, 945
- Balsara, D. S., Käppeli, R., Boscheri, W., & Dumbser, M. 2021, *CAMCS*, **5**, 235
- Balsara, D. S., Samantary, S., & Subramanian, S. 2023b, *CAMCS*, **5**, 428
- Balsara, D. S., & Shu, C.-W. 2000, *JCoPh*, **160**, 405
- Balsara, D. S., & Spicer, D. S. 1999, *JCoPh*, **149**, 270
- Baumgarte, T. W., Brügmann, B., Cors, D., et al. 2023a, *PhRvL*, **131**, 181401
- Baumgarte, T. W., Gundlach, C., & Hilditch, D. 2023b, *PhRvD*, **107**, 084012
- Baumgarte, T. W., & Hilditch, D. 2022, *PhRvD*, **106**, 044014
- Baumgarte, T. W., & Shapiro, S. L. 1998, *PhRvD*, **59**, 024007
- Baumgarte, T. W., & Shapiro, S. L. 2010, *Numerical Relativity: Solving Einstein’s Equations on the Computer* (Cambridge: Cambridge Univ. Press)
- Berberich, J. P., Chandrasekar, P., & Klingenberg, C. 2021, *CF*, **219**, 104858
- Bermudez, A., & Vázquez-Cendón, M. 1994, *CF*, **23**, 1049
- Berti, E., Cardoso, V., & Starinets, A. O. 2009, *CQGra*, **26**, 163001
- Beyer, H., & Sarbach, O. 2004, *PhRvD*, **70**, 104004
- Bhoriya, D., Balsara, D. S., & Shu, C.-W. 2024, *JSCoM*, submitted
- Bona, C., Ledvinka, T., Palenzuela, C., & Záček, M. 2003, *PhRvD*, **67**, 104005
- Bona, C., Ledvinka, T., Palenzuela, C., & Záček, M. 2004, *PhRvD*, **69**, 64036
- Bona, C., & Palenzuela-Luque, C. 2005, *Elements of Numerical Relativity* (Berlin: Springer-Verlag)
- Borges, R., Carmona, M., Costa, B., & Don, W. S. 2008, *JCoPh*, **227**, 3191
- Botta, N., Klein, R., Langenberg, S., & Lützenkirchen, S. 2004, *JCoPh*, **196**, 539
- Boyle, M., Lindblom, L., Pfeiffer, H. P., Scheel, M. A., & Kidder, L. E. 2007, *PhRvD*, **75**, 024006
- Brill, D. R., & Lindquist, R. W. 1963, *PhRv*, **131**, 471
- Brown, J. D., Diener, P., Field, S. E., et al. 2012, *PhRvD*, **85**, 084004
- Brügmann, B. 2013, *JCoPh*, **235**, 216

- Brügmann, B., González, J. A., Hannam, M., et al. 2008, [PhRvD](#), **77**, 024027
- Cai, X., & Ladeinde, F. 2008, in in 46th AIAA Aerospace Sciences Meeting and Exhibit (Reston, VA: ARC), [AIAA](#) 2008–36
- Calabrese, G., Hinder, I., & Husa, S. 2006, [JCoPh](#), **218**, 607
- Castro, M. J., de Luna, T. M., & Parés, C. 2017, *Handbook of Numerical Analysis*, Vol. 18 (Amsterdam: Elsevier), 131
- Castro, M. J., & Pares, C. 2020, [JSCoM](#), **82**, 1
- Clough, K., Figueras, P., Finkel, H., et al. 2015, [CQGra](#), **32**, 245011
- Colella, P., & Woodward, P. R. 1984, [JCoPh](#), **54**, 174
- Cravero, I., & Semplice, M. 2016, [JSCoM](#), **67**, 1219
- de Felice, F., & Clarke, C. J. S. 1990, *Relativity on Curved Manifolds* (Cambridge: Cambridge Univ. Press)
- Dedner, A., Kemm, F., Kröner, D., et al. 2002, [JCoPh](#), **175**, 645
- Del Zanna, L., Zanotti, O., Bucciantini, N., & Londrillo, P. 2007, [A&A](#), **473**, 11
- Deppe, N., Foucart, F., Bonilla, M. S., et al. 2024, [arXiv:2406.19038](#)
- Duez, M. D., Foucart, F., Kidder, L. E., et al. 2008, [PhRvD](#), **78**, 104015
- Dumbser, M., & Balsara, D. S. 2016, [JCoPh](#), **304**, 275
- Dumbser, M., Fambri, F., Gaburro, E., & Reinartz, A. 2020, [JCoPh](#), **404**, 109088
- Dumbser, M., Guercilena, F., Köppel, S., Rezzolla, L., & Zanotti, O. 2018, [PhRvD](#), **97**, 084053
- Dumbser, M., Zanotti, O., Gaburro, E., & Peshkov, I. 2024, [JCoPh](#), **504**, 112875
- Dumbser, M., Zanotti, O., Hidalgo, A., & Balsara, D. S. 2013, [JCoPh](#), **248**, 257
- Faber, J. A., Baumgarte, T. W., Etienne, Z. B., Shapiro, S. L., & Taniguchi, K. 2007, [PhRvD](#), **76**, 104021
- Gaburro, E., Castro, M. J., & Dumbser, M. 2021, [SJSC](#), **43**, B1226
- Gosse, L. 2001, [Math. Models Methods Appl. Sci.](#), **11**, 339
- Gourgoulhon, E. 2012, *3+1 Formalism in General Relativity* (Berlin: Springer)
- Gowdy, R. H. 1971, [PhRvL](#), **27**, 826
- Gundlach, C., Calabrese, G., Hinder, I., & Martin-Garcia, J. M. 2005, [CQGra](#), **22**, 3767
- Harten, A., Osher, S., Engquist, B., & Chakravarthy, S. R. 1986, [ApNM](#), **2**, 347
- Henrick, A. K., Aslam, T. D., & Powers, J. M. 2006, [JCoPh](#), **213**, 311
- Hilditch, D., Bernuzzi, S., Thierfelder, M., et al. 2013, [PhRvD](#), **88**, 084057
- Hilditch, D., & Richter, R. 2012, [PhRvD](#), **86**, 123017
- Hu, X. Y., Adams, N. A., & Shu, C.-W. 2013, [JCoPh](#), **242**, 169
- Inghirami, G., Del Zanna, L., Beraudo, A., et al. 2016, [EPJC](#), **76**, 659
- Jiang, G.-S., & Shu, C.-W. 1996, [JCoPh](#), **126**, 202
- Jiang, Y., Shu, C.-W., & Zhang, M. 2013, [SJSC](#), **35**, A1137
- Jiang, Y., Shu, C.-W., & Zhang, M. 2014, [MApAn](#), **21**, 1
- Jiménez-Vázquez, E., & Alcubierre, M. 2022, [PhRvD](#), **106**, 044071
- Käppeli, R. 2022, [LRCA](#), **8**, 2
- Kerr, R. P. 1963, [PhRvL](#), **11**, 237
- Kidder, L. E., Scheel, M. A., & Teukolsky, S. A. 2001, [PhRvD](#), **64**, 064017
- Kiuchi, K., Kawaguchi, K., Kyutoku, K., et al. 2017, [PhRvD](#), **96**, 084060
- LeVeque, R. J. 1998, [JCoPh](#), **146**, 346
- Levy, D., Puppo, G., & Russo, G. 2000, [ApNM](#), **33**, 415
- Lindblom, L., Scheel, M. A., Kidder, L. E., Owen, R., & Rinne, O. 2006, [CQGra](#), **23**, S447
- Löffler, F., Faber, J., Bentivegna, E., et al. 2012, [CQGra](#), **29**, 115001
- Lousto, C. O., & Healy, J. 2023, [CQGra](#), **40**, 09LT01
- Lück, H., Smith, J., & Punturo, M. 2022, *Third-Generation Gravitational-Wave Observatories* (Singapore: Springer), 283
- Mamani, L. A. H., Masa, A. D. D., Sanches, L. T., & Zanchin, V. T. 2022, [EPJC](#), **82**, 897
- Merriman, B. 2003, [JSCoM](#), **19**, 309
- Munz, C.-D., Omnes, P., Schneider, R., Sonnendrücker, E., & Voss, U. 2000, [JCoPh](#), **161**, 484
- Nakamura, T., Oohara, K., & Kojima, Y. 1987, [PThPS](#), **90**, 1
- Nonomura, T., Iizuka, N., & Fujii, K. 2010, [CF](#), **39**, 197
- Pareschi, L., & Rey, T. 2017, [CF](#), **156**, 329
- Peterson, A. J., Willcox, D., & Mösta, P. 2023, [CQGra](#), **40**, 245013
- Rezzolla, L., & Zanotti, O. 2013, *Relativistic Hydrodynamics* (Oxford: Oxford Univ. Press)
- Scheel, M. A., Boyle, M., Chu, T., et al. 2009, [PhRvD](#), **79**, 024003
- Schwarzschild, K. 1916, *SPAW*, **189**
- Shibata, M., & Nakamura, T. 1995, [PhRvD](#), **52**, 5428
- Shu, C.-W., & Osher, S. 1988, [JCoPh](#), **77**, 439
- Shu, C.-W., & Osher, S. 1989, [JCoPh](#), **83**, 32
- Spiteri, R. J., & Ruuth, S. J. 2002, [SJNA](#), **40**, 469
- Spiteri, R. J., & Ruuth, S. J. 2003, [Math. Comput. Simul.](#), **62**, 125
- Szilágyi, B. 2014, [IJMPD](#), **23**, 1430014
- Thierfelder, M., Bernuzzi, S., & Brügmann, B. 2011, [PhRvD](#), **84**, 044012
- Tichy, W. 2009, [PhRvD](#), **80**, 104034
- Tichy, W., Ji, L., Adhikari, A., Rashti, A., & Pirog, M. 2023, [CQGra](#), **40**, 025004
- Wiltshire, D. L., Visser, M., & Scott, S. M. 2009, *The Kerr Spacetime* (Cambridge: Cambridge Univ. Press)
- Wu, K., & Tang, H. 2015, [JCoPh](#), **298**, 539
- Xing, Y., & Shu, C.-W. 2011, [AdWR](#), **34**, 1026
- Yamamoto, T., Shibata, M., & Taniguchi, K. 2008, [PhRvD](#), **78**, 064054
- Zheng, F., Shu, C.-W., & Qiu, J. 2021, [JCoPh](#), **445**, 110597
- Zhu, J., & Qiu, J. 2016, [JCoPh](#), **318**, 110
- Zhu, J., & Shu, C.-W. 2018, [JCoPh](#), **375**, 659
- Zlochower, Y., Baker, J. G., Campanelli, M., & Lousto, C. O. 2005, [PhRvD](#), **72**, 024021